The Pennsylvania State University

The Graduate School

Department of Materials Science and Engineering

DIELECTRIC BREAKDOWN OF ALKALI-FREE BOROALUMINOSILICATE GLASS THIN FILMS

A Thesis in

Materials Science and Engineering

by

Jessica Lynn Serra

Submitted in Partial Fulfillment
of the Requirements
for the Degree of

Master of Science

August 2010

The thesis of Jessica Lynn Serra was reviewed and approved* by the following:

Carlo G. Pantano
Distinguished Professor of Materials Science and Engineering
Thesis Co-Advisor

Michael T. Lanagan
Professor of Engineering Science and Mechanics
Thesis Co-Advisor

Mark W. Horn
Associate Professor of Engineering Science and Mechanics

Nikolas J. Podraza
Research Assistant Professor of Electrical Engineering

Joan M. Redwing
Professor of Materials Science and Engineering
Chair, Intercollege Graduate Degree Program in Materials Science and Engineering

*Signatures are on file in the Graduate School

ABSTRACT

Some glasses have exhibited dielectric breakdown strengths two orders of magnitude higher than polycrystalline ceramic materials. Their high dielectric breakdown strength makes glass an ideal candidate for use in high energy density capacitors for pulsed power applications.

It has been observed in recent studies that a commercial alkali-free boroaluminosilicate glass, Schott AF45^{TM}, exhibits a dielectric breakdown strength of 12-13 MV/cm. In order to successfully measure the dielectric breakdown strength of this glass, samples 5-30 microns thick were used during testing. It was desirable to continue testing glass below 5 microns thick in the pursuit of measuring the intrinsic dielectric breakdown strength. In this study, thin film deposition was used to produce glass less than 5 microns thick. Because of a built-in thickness gradient in the films across the wafer surface, each sample provided a range of thicknesses to measure.

AF45 was used as the target material. RF magnetron sputtering was chosen over other deposition techniques, such as evaporation or chemical vapor deposition, because of its ability to sputter insulators, the ability to use a piece of commercial glass as the target material, the increased film density and good compositional control.

Several characterization techniques were used to understand the properties of the films. The films were examined with field emission scanning electron microscopy and observed to be microstructure free. The composition, measured by x-ray photoelectron spectroscopy, differed from that of the bulk glass. The films also appear to have a

significant amount of water included in the structure and a lower density based on spectra obtained from Fourier transfer infrared spectroscopy measurments.

The dielectric breakdown strength of the films was measured to be 9.5-10 MV/cm, about 20% lower then the dielectric breakdown strength of the thinnest sample of bulk glass. The decreased breakdown strength measured for the thin films is attributed to several factors. The presence of water and the low density of the films can allow for charge to pass through the glass films more easily than in the bulk. Microstructural defects such as voids and impurities within the deposited film, electrodes and especially at the film/electrode interface, are obvious candidates based upon previous work with bulk dielectrics. The compositional non-uniformity observed in the films could further enhance structural defect formation, beyond those intrinsic to the deposition process itself.

TABLE OF CONTENTS

LIST OF FIGURES vi

LIST OF TABLES ix

ACKNOWLEDGEMENTS x

CHAPTER 1 INTRODUCTION 1

CHAPTER 2 LITERATURE REVIEW 5

2.1 GLASS THIN FILMS 5
2.2 TECHNIQUES USED IN GLASS THIN FILM DEPOSITION 5
2.3 RADIO FREQUENCY (RF) MAGNETRON SPUTTERING 7
2.4 SPUTTER YIELD 11
2.5 DIELECTRIC BREAKDOWN 12

CHAPTER 3 EXPERIMENTAL METHODS 18

3.1 THIN FILM SYNTHESIS 18
3.2 COMPOSITIONAL ANALYSIS 23
3.3 OPTICAL SPECTROSCOPY 25
3.4 PROFILOMETRY AND MICROSCOPY 30
3.5 DIELECTRIC BREAKDOWN TESTING 31

CHAPTER 4 RESULTS AND DISCUSSION 34

4.1 THIN FILM CHARACTERIZATION 34
4.1.1 Microstructure 34
4.1.2 Composition 43
4.1.3 Structure 47
4.2 DIELECTRIC BREAKDOWN DATA 54
4.3 DIELECTRIC BREAKDOWN COMPARISON 68

CHAPTER 5 SUMMARY AND LESSONS LEARNED 72

APPENDIX A ADDITIONAL THICKNESS MAPS 75

APPENDIX B COMPOSTIONAL DATA 78

APPENDIX C DIELECTRIC BREAKDOWN EVENTS 79

BIBLIOGRAPHY 84

LIST OF FIGURES

Figure **2.1**: Schematic diagram illustrating one example of a radio frequency sputter deposition processing chamber 10

Figure **2.2**: Schematic diagram of a sputter deposition processing chamber with the addition of a planar magnetron. The magnetic field lines are shown to indicate the path electrons are forced to take 10

Figure **2.3**: A current versus voltage curve of an ideal dielectric material, adapted from Solymar 12

Figure **3.1**: A diagram of a Kurt J. Lesker CMS-18 magnetron sputter deposition system. The system can run 3 different targets at once, two guns are radio frequency and one gun is direct current. The gun on the right is shown raised 19

Figure **3.2**: Thickness distribution of film 02/08 measured across a 4 inch wafer, achieved by the deposition technique described in Section 3.1. 20

Figure **3.3**: Representation of a thin film sample, top view, after deposition of glass and electrodes. The colors in the figure resemble the colors observed on the thin film due to light interference. 22

Figure **3.4**: Casa XPS regions and components needed to fit the B 1s peak. Spectrum was taken from a bulk AF45 vacuum fracture surface 25

Figure **3.5**: A five medium structural model used to represent the glass thin films during modeling of thickness and optical properties 28

Figure **3.6**: Average optical dispersion curve for AF45 thin films on platinum generated with ellipsometry measurements and modeling. This information was programmed into the reflectometry analysis software 28

Figure **3.7**: Illustration of how the surface of a thin film is measured at a glancing angle in FE-SEM 31

Figure **3.8**: Photograph of the dielectric breakdown test configuration with thin film sample. The copper plate is the anode and the steel probe is the cathode. 32

Figure **3.9**: Schematic of the dielectric breakdown test configuration with thin film sample.....33

Figure **4.1**: Field emission scanning electron microscopy image of film 12/10 in cross section. The top layer is glass, the light layer in the center is platinum and the bottom layer is the silicon substrate.....35

Figure **4.2**: a) FE-SEM image of the surface of film 12/10 at an angle of 90˚. B) FE-SEM image of the same spot at an angle of 20˚ which highlights some surface roughness. Both images were taken at the same magnification 37

Figure **4.3**: Surface profile taken from film 10/14 approximately representing the average roughness value. The RMS roughness in the figure is 0.67 nm 38

Figure **4.4**: Surface profile taken from a 46.8 micron thick piece of as received AF45 having the average roughness value, 0.30 nm 39

Figure **4.5**: Surface profile taken from a piece of AF45 etched in 5% HF for 5 minutes. The sample shown has an initial thickness of 46.5 microns and a final thickness of 34.1 microns. This sample was chosen to represent the average roughness value of etched AF45. The RMS roughness in the figure is 0.65 nm.....39

Figure **4.6**: Thickness map of film 11/18 showing a 3D view of the thickness distribution... 41

Figure **4.7**: Thickness map of film 11/18 showing the top view of the sample. 41

Figure **4.8**: Thickness map of film L2 showing a 3D view of the thickness distribution 42

Figure **4.9**: Thickness map of film L2 showing the top view of the sample 42

Figure **4.10**: XPS survey scan comparison of a bulk AF45 vacuum fracture surface (red) and film 12/10 (green) 45

Figure **4.11**: Dispersion curves measured using ellipsometry from film 11/05.....48

Figure **4.12**: Dispersion curve of the average film, measured at 70 degrees, and bulk AF45, measured at 50 degrees. 49

Figure **4.13**: Thickness (Å) measured with ellipsometry compared to the respective refractive index calculated for each point at 240 nm.....50

Figure **4.14**: FTIR spectra taken with ATR of bulk AF45 (red) and film 12/10 (blue) 51

Figure **4.15**: FTIR spectra taken with ATR and reflectance of bulk AF45 showing the difference in peak location and shape depending on the measurement technique. 52

Figure **4.16**: FTIR spectra taken in reflection mode of film 12/10 before and after annealing 53

Figure **4.17**: All useable data points, taken in the initial test, plotted as breakdown strength (MV/cm) versus thickness (cm). The plot does not include data with a breakdown voltage ≤ 604 V 54

Figure **4.18**: Log [Characteristic strength (V/m)] vs. Log [Thickness (microns)] of test and retest values. The thicknesses are averaged from all of the data within each film 56

Figure **4.19**: Weibull moduli for two data sets, breakdown spots below 0.99 microns and above 4.50 microns. These data sets were chosen to compare a high Weibull modulus distribution and a low Weibull modulus distribution 58

Figure **4.20**: Log [Characteristic strength (V/m)] vs. Log [Thickness (microns)] of test and retest values. The thicknesses are averaged from all of the data within each thickness interval 59

Figure **4.21**: FE-SEM cross section of a breakdown event 61

Figure **4.22**: FE-SEM and optical microscope image of a breakdown event on a sample 1.04 microns thick that broke down at 1139 V 62

Figure **4.23**: FE-SEM and optical microscope image of a breakdown event on a sample 0.98 microns thick that broke down at ≤ 543 V 63

Figure **4.24**: FE-SEM and optical microscope image of a breakdown event on a sample 3.07 microns thick that broke down at 3905 V 64

Figure **4.25**: FE-SEM and optical microscope image of a breakdown event on a sample 3.03 microns thick that broke down ≤ 497 V 65

Figure **4.26**: Log [Characteristic strength (V/m)] vs. Log [Thickness (microns)] of bulk glass characteristic strength taken from Table 4.6 and 4.7 and thin film test values from Table 4.4. The thin film thicknesses are averaged from all of the data within each thickness interval 68

LIST OF TABLES

Table **3.1**: Thin film sample designations 22

Table **4.1**: Average RMS roughness (nm) of the surfaces of as received bulk AF45, etched bulk AF45 and several thin films 38

Table **4.2**: Compositions taken by XPS and EPMA of several films fabricated at Penn State and at the Kurt. J. Lesker Company. Bulk glass values are also included for comparison 44

Table **4.3**: Percent difference of the film spots with each other and of the films compared to bulk AF45. 46

Table **4.4**: Breakdown field values and corresponding Weibull moduli for data sets consisting of all test spots on a particular sample. Values for initial test and retest are displayed 56

Table **4.5**: Breakdown field values and corresponding Weibull moduli for data sets consisting of all test spots within a particular thickness range. Values for initial test are displayed 58

Table **4.6**: Breakdown field values and corresponding Weibull moduli for data sets consisting of all test spots within a particular thickness range. Values for retests are displayed 59

Table **4.7**: Weibull moduli and characteristic strength values of bulk glass taken from the Lee paper. 66

Table **4.8**: Weibull moduli and characteristic strength values of bulk glass taken from the Smith paper 67

ACKNOWLEDGEMENTS

There are so many people I want to thank that have helped me survive the challenging IUG thesis project process. First of all I would like to thank Dr. Pantano and Dr. Lanagan for agreeing to take me on as a student and for offering insight and guidance that will stay with me for the rest of my life. I would also like to thank Dr. Horn and Dr. Podraza for completing my committee. Dr. Horn has been another great mentor whose unique approach to teaching and research has complimented the styles of my co-advisors. Nik Podraza has been an integral part of the work I've done by offering his expertise in optical measurement techniques and his own philosophies on all things involving or not involving research. I really appreciate his enthusiasm and willingness to teaching me about ellipsometry and reflectometry. The passion for research and excitement to learn new things I see in these educators has inspired me to pursue my own research interests with just as much enthusiasm as they pursue theirs.

I would like to thank Bill Drawl for his infinite patience with me every time I thought I broke something on the deposition tool and his wisdom about life, the future and softball. The Materials Characterization Laboratory staff, especially Josh, Vince, John, Jeff and Mark, has helped in one way or the other with data analysis and research advice and I am extremely grateful for their help.

Thank you to my fellow CGP grad students, Jen, Nick and Joy for always lending a helping hand and for just being awesome people. It has been wonderful working alongside such intelligent, driven individuals.

Without April, Donna, Allison, Jenneth and Dr. Kimel I would not have been able to successfully wade through the paperwork and the intricacies of the graduation process. I appreciate each and every one of them both professionally and personally for being so helpful and kind throughout my time at Penn State. The Materials Science and Engineering department is one of a kind for helpful people, cutting edge research, and a memorable college experience and I'm eternally grateful to have had the opportunity to be here for the past 5 years.

Last but not least I want to thank my loving family and friends for their encouragement and support throughout everything I've experienced in the last few years. I could not have survived the epic challenges I have faced without their presence in my life.

This research was possible through funding by the Department of Energy and the National Science Foundation's International Materials Institute.

CHAPTER 1

INTRODUCTION

The dielectric breakdown strength of glass can be significantly higher than that of the polycrystalline ceramics used in capacitors [1-5]. Borosilicate glasses such as Pyrex have been observed to have dielectric breakdown strengths around 9 MV/cm [6-8] whereas $BaTiO_3$ has a dielectric breakdown strength two orders of magnitude lower [9-11] There are several extrinsic factors that contribute to lowering the dielectric breakdown strength of polycrystalline materials such as grain boundaries, pores and anisotropic permittivity in randomly oriented crystals [12]

High-quality, commercial, alkali-free boroaluminosilicate wafer glasses are being studied for use in high energy density capacitors because of their high dielectric breakdown strength [13, 14]. High energy density capacitors can be used in life saving implantable medical devices and fuel efficient hybrid electric vehicles.

Having been developed for flat screens and portable electronics, commercial glasses are now readily available and sufficiently thin to investigate their dielectric properties. The increased availability of this glass reduces the cost which can translate to cheaper capacitors in the future. This study looks at taking commercial glass and directly integrating it into the thin film deposition process as a target material, a step which could lead to additional cost reduction during future manufacturing of thin film glass capacitors.

Environmentally, glasses are an ideal material to use since they are readily recycled. Alkali-free boroaluminosilicate glasses do not contain significant quantities of harmful elements. Though the glass used in this study contained about 0.5 mol% As_2O_3, used as a fining agent, it has ceased to be used; the next generation of this glass contains no As_2O_3 or other hazardous materials.

It is desirable to have thin glass with a pristine melt surface to avoid cracks and flaws which could lead to a lower dielectric breakdown strength than is intrinsic to the material [3]. It has been observed that dielectric breakdown is inversely proportional to thickness as it approaches the intrinsic dielectric breakdown strength of the solid [13, 15, 16]. In order to extend our investigation of dielectric breakdown we need to obtain or fabricate thinner and thinner glasses. Having a method to fabricate high quality, thin glass is also beneficial to the manufacturing of more compact capacitors.

In the past, the thin glass needed to measure intrinsic dielectric breakdown strength was obtained by blowing the glass into bubbles, cutting it and measuring the thickness [17] or by grinding and polishing larger pieces to the desired thickness [15]. The thickness of blown glass is difficult to control and the pieces tend to be curved. Grinding and polishing is time consuming and alters the surface of the glass.

In previous studies, thin boroaluminosilicate wafer glasses, 30-50 microns thick, were thinned in hydrofluoric (HF) acid [13, 14]. HF acid roughens the surface slightly and changes the surface composition of the glass. When a silicate is submerged in HF acid, in addition to dissolution of the Si-O bonds, the bonds between network intermediates and oxygen will break at different rates. Leaching of modifier will also occur. This can lead to an altered surface layer both in composition and in structure [18].

It would be ideal to have a pristine glass melt surface less than 5-10 microns thick in order to continue the work done in the previously mentioned studies.

The approach taken in this study is to fabricate glass thin films in order to extend the study of alkali-free boroaluminosilicate glasses below 5 microns, which is the limit for etched bulk glass [13, 14]. Thin film capacitors have been successfully fabricated and tested by many other researchers. Their methods used to fabricate multi-component glass capacitors have often involved co-sputtering of composite targets or multiple powder targets [19-22]. The use of a commercial piece of bulk glass as the target material, instead of a pressed powder target or multiple oxide targets, is explored in this study. The physical properties as well as the dielectric breakdown strength are studied and compared to the properties of the bulk glass.

Since dielectric breakdown is a statistical process [23], it is beneficial to have many test spots to measure. The thin films fabricated for this research allow for many tests to be conducted per sample. Films with a thickness gradient were fabricated in order to measure breakdown over a range of thicknesses below 5 microns with only a single wafer needing to be processed.

Radio frequency (RF) magnetron sputter deposition was chosen as the film fabrication technique for several reasons: the ability to use commercial glass as a target material, the ability of the technique to deposit insulators, the high density of films compared to other deposition methods, the better compositional match of films to the target material and control of deposition parameters [24-27]. RF magnetron sputter deposition is also an ideal technique for large scale production since it can be scaled up for manufacturing [28]. Large scale film deposition has already been integrated into

industries such as window glass with coatings for reduction of energy loss [29]. Despite all of the benefits to using RF magnetron sputter deposition, challenges were encountered limiting some aspects of sample fabrication.

Chapter 2 will provide a brief background of RF magnetron sputter deposition as well as other techniques traditionally used to deposit glass as a thin film. The benefits of the technique along with the anticipated challenges, such as the low sputter yield of an oxide target, will also be discussed in more detail. The principles behind dielectric breakdown and the behavior of glass under applied voltage will be described.

Chapter 3 outlines the procedures used in this study to fabricate, characterize and test the dielectric breakdown strength of the films.

In Chapter 4 the films will be described in detail based on their characterization and dielectric breakdown testing results. The characteristics of the bulk glass, which will act as a basis for comparison with the films, will also be described. The dielectric breakdown performance of the films and the bulk glass will be compared and discussed.

A summary of the work done in this study as well as some lessons learned throughout the process will be included in Chapter 5.

CHAPTER 2

LITERATURE REVIEW

2.1 GLASS THIN FILMS

In early semi-conductor research, SiO_2 films were used for device passivation and insulation of active devices [30-33]. Because of the limitations of thermally grown oxides such as a self limiting thickness and the desire for a high quality oxide film on non-silicon surfaces, investigators worked on developing reliable methods to deposit thin glass insulating films [32]. Glass thin films have also been used for optical coatings [34, 35] and devices such as wave guides [36], interference stacks [35] and optical switches [37].

Research has been conducted on the best way to deposit thin film capacitors with glasses in order to reduce the size of integrated circuits while utilizing the excellent dielectric properties of glass [2, 19, 38]. The ability to have a thin dielectric material also makes it possible to test dielectric breakdown strength at reasonable voltages.

2.2 TECHNIQUES USED IN GLASS THIN FILM DEPOSITION

Thin films are fabricated in a variety of different ways. Glass films have most commonly been deposited using chemical vapor deposition (CVD), evaporation and sputter deposition. All thin film deposition techniques utilize at least one of the following

parameters to control the outcome of the thin film: temperature, bombardment or chemistry.

CVD is possible through careful control of process gas chemistry. Starting materials are in the form of volatile gasses that are thermally decomposed allowing the material to deposit on the substrate. Silica films are often made by reacting SiH_4 in the presence of oxygen at high temperatures. The films typically fabricated using CVD are single component materials such as Si, TiO_2 and BN. CVD is most useful when coating oddly shaped or large substrates especially when uniformity is critical. It is utilized as a high throughput technique with the ability to do large batches and deposit at high rates [25, 27].

Despite the benefits of this technique, it would be unsuitable for deposition of multi-component films. The complex gas mixture that would be needed to synthesize a multi-component glass would be difficult to obtain and control. Additionally the precursor gasses are often toxic and corrosive and when decomposed may leave trace amounts of impurities in the film [25, 27].

Evaporation requires low pressures and high temperatures to vaporize the source material onto a substrate without the assistance of ion bombardment. In evaporation, material is sublimated by resistive heating or electron beam heating. Depending on the substrate holder design, such as a rotating planetary holder, evaporated films have the potential to be very uniform [27].

Several factors eliminated evaporation as the primary method for multi-component glasses. Glass films deposited by evaporation tend to be less dense than the target material. Evaporation is notorious for producing films with compositions that differ

from the bulk material due to the different vapor pressures of elements in a compound [27, 31]. An example of incongruent vaporization is SiO_2 which can deposit as a combination of SiO, SiO_2 and Si_2O_3 [34].

Thin films do not always exhibit the properties of their bulk counterparts. Deposition is a non-equilibrium process and therefore may yield a metastable material that cannot be fabricated with other methods. Depending on the situation, the thin film can have new or enhanced properties, or they can have degraded properties.

This study will focus on films fabricated by radio frequency magnetron sputter deposition. The following section outlines the advantages and disadvantages of the technique and why it was chosen to deposit alkali-free boroaluminosilicate glass thin films.

2.3 RADIO FREQUENCY (RF) MAGNETRON SPUTTERING

The primary deposition technique used in this study to fabricate alkali-free boroaluminosilicate glass thin films is radio frequency (RF) magnetron sputter deposition. The primary goal is to prepare films 1-5 microns thick to further explore the thickness dependence of dielectric breakdown in this glass [13, 15, 16, 39]. Identifying deposition conditions and processes to fabricate high quality alkali-free boroaluminosilicate glass films will be useful in the future for producing high energy density thin film capacitors and other devices.

Sputter deposition utilizes transfer of momentum through ion bombardment to vaporize a target material. The vaporized material diffuses through a plasma and is

deposited on a substrate. There are numerous versions of sputter deposition techniques, such as reactive, ion beam and direct current sputtering.

RF magnetron sputter deposition is ideal for sputtering insulating materials. Figure 2.1 illustrates an example of a radio frequency sputter deposition system. In a direct current configuration when a voltage is applied across the target, positive charge would build up on the surface of an insulating material, preventing the plasma from being sustained and effectively halting deposition. In most conventional RF systems, the voltage is alternated at a frequency of 13.56 MHz with an asymmetrical plasma configuration. In this configuration the target acts as the 'driven electrode' while the substrate and all of the surfaces inside the processing chamber act as the grounded electrode. Since the electrons are much lighter than the plasma ions, they are able to oscillate with the field and neutralize the positive charge as it builds up on the electrodes. The size difference of the electrodes prevents the alternating currents from sputtering both electrodes by driving the target, the smaller electrode, to a negative bias so that ion bombardment is concentrated there [22, 24].

In addition to the ability to sputter deposit insulators and a variety of other materials despite their degree of refractoriness, RF sputtering allows for lower voltages and system pressures than in direct current sputter deposition since electron oscillations increase the ionizing collisions within the plasma, maintaining its density [22, 24].

Magnetron sputtering also helps to further decrease the pressure and the voltage needed to sustain the plasma. The cross product of the electric and magnetic fields forces electrons to spiral close to the target, increasing ionization of the gas near the target and therefore increasing the ion bombardment. A decrease in the pressure also leads to less

gas molecules trapped in the film, avoiding unnecessary contamination by plasma gas species [22, 24]. Figure 2.2 illustrates the path electron take in a magnetron system.

There are many deposition parameters to vary in order to achieve the best film for the desired application. Pressure, target-to-substrate distance, process gas, substrate temperature, target material and operation power must all be considered [22, 24]. The variables chosen in this study resulted from reviewing the literature and observing the limitations of the equipment and target materials to achieve the best possible samples.

One of the limitations of an insulating target material is a low deposition rate [24]. In order to increase deposition rate, power density must be increased. Since the glass is susceptible to thermal shock there was a limited amount of power that could be applied to the target. If the target was run at too high of a power, it would crack and the copper backing plate would be exposed to the plasma allowing it to also be sputtered.

There are several reasons to justify the use of RF magnetron sputter deposition to fabricate the films for this study. The ability to use a solid piece of commercial multi-component glass as the target material can reduce costs and eliminate the step of pressing and sintering a target. RF magnetron sputter deposition also gives the user precise control over the plasma chemistry and can obtain films with better structural and stoichiometric agreement to the target material than by using evaporation or chemical vapor deposition.

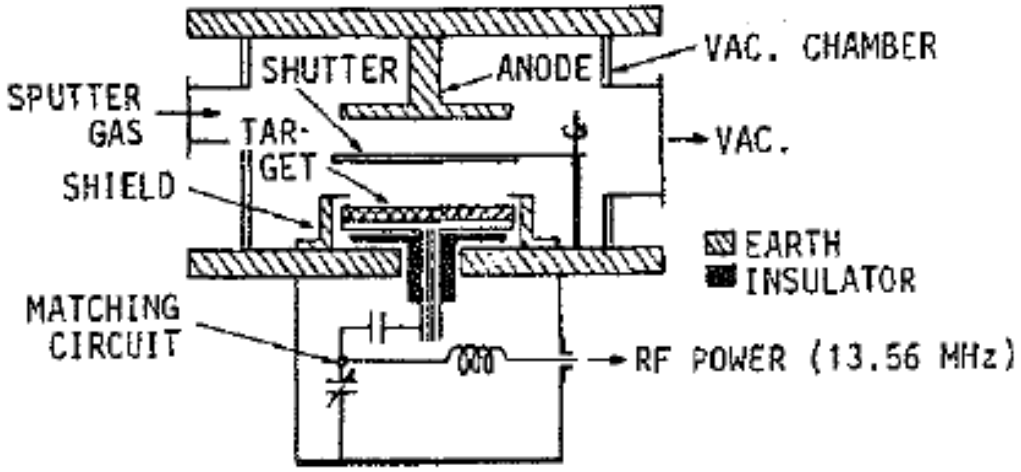

Figure 2.1: Schematic diagram illustrating one example of a radio frequency sputter deposition processing chamber. [22]

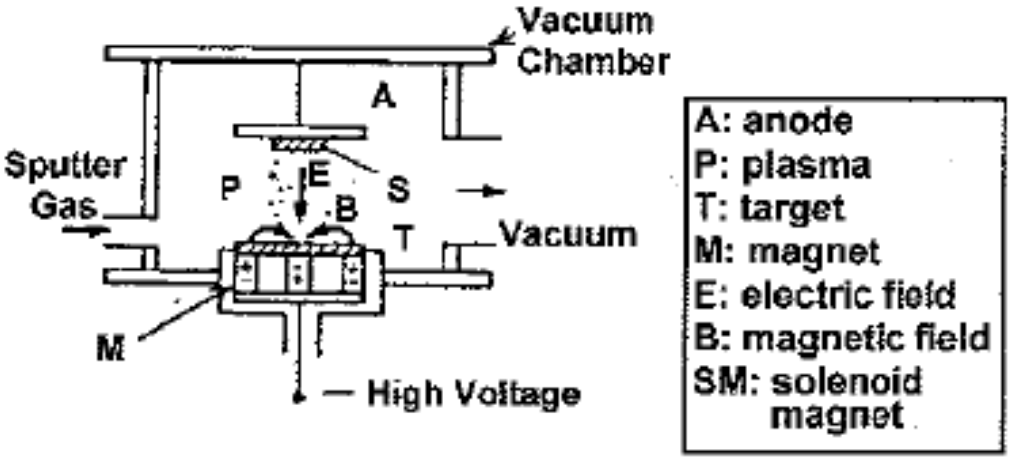

Figure 2.1: Schematic diagram of a sputter deposition processing chamber with the addition of a planar magnetron. The magnetic field lines are shown to indicate the path electrons are forced to take. [22]

2.4 SPUTTER YIELD

The sputter yield, which is the ratio of atoms removed from the target material to bombarding ions, of each atomic species within the glass is different. It is important to understand how a material will behave during bombardment in order to understand how it will deposit as a film. Sputter yield depends on factors such as size, energy and angle of incidence of the bombarding atoms, pressure and the nature of bonding within the target material. The sputter yields of single component materials is well documented under a series of different deposition conditions [40]. There has also been work looking at the sputter yields of some metallic alloys and simple oxides. It has been observed that oxides have a lower yield than their single component metallic counterparts [22, 24, 26].

In multi-component systems such as this glass, the composition of the film should be equivalent to the composition of the target material despite differences in individual atom sputter yield. To ensure that this occurs, targets are sputtered until they reach a steady state surface composition. The elements with a high sputter yield will become depleted on the target surface while the elements with a low sputter yield will become enriched. The disproportional target composition will now yield deposited films with the same composition as the starting target material since the high sputter yield atoms become difficult to remove from the target and the lower yield atoms become more accessible. This is most often observed in metallic alloys [22, 24].

2.5 DIELECTRIC BREAKDOWN

Glasses are typically electrically insulating materials. In some cases it can be observed that if a potential is applied across a piece of glass, the ions will carry the charge [5, 29]. Ion conduction is orders of magnitude less than electron conduction due to the lower mobility of such ions. In order for the glass network to allow ion conduction to occur more easily, alkali ions have to break up the network and create non bridging oxygen [29]. In an alkali-free glass, like the ones discussed in this study, the network should not allow significant ion motion since there are large divalent cations instead of the more mobile alkali ions. Without the possibility of significant ion motion, and electronic conduction limited by the high band gap of the network, only impurities and point defects are expected to contribute to conduction [29].

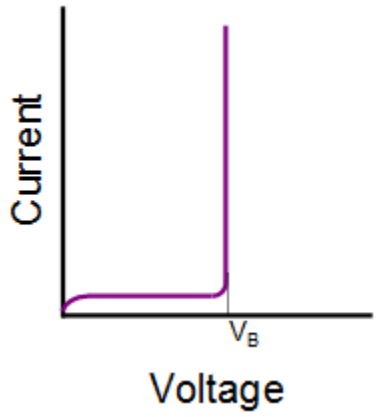

Figure 2.3: A current versus voltage curve of an ideal dielectric material, adapted from Solymar. [41]

In glasses and other dielectric materials, dielectric breakdown is said to occur when the conduction of the material sharply increases [3, 5]. In a thin, ideal dielectric the

current-voltage behavior would look like Figure 2.3. Initially little current flows through the material, the rapid rise in current coincides with the breakdown event occurring at V_B. In a non-ideal dielectric the current rises gradually until breakdown occurs, often the non-linear part of the curve at the high voltage range, in Figure 2.3, is not observable for thick (>1 micron) dielectrics due to catastrophic failure during breakdown.

The dielectric breakdown of insulating materials behaves in a 'weakest link' manner. When the material is stressed, it is most probable that the failure will be initiated by the weakest part of the material, for example: point defects, mobile impurities and microstructural defects. Dielectric breakdown is analogous to mechanical failure of ceramic materials. These types of behavior are best understood by applying Weibull statistics [23, 42].

The study of dielectric breakdown is important to the development of high energy density materials because of the relationship between them, described in Equation 2.1. Energy density, u, is proportional to the square of breakdown field, E, of a material where ε is the permittivity of free space, ε_r is the permittivity of a material and E is the field.

$$u = \tfrac{1}{2} \varepsilon \varepsilon_r E^2 \qquad [2.1]$$

High dielectric breakdown strength affects the energy density at a higher rate than permittivity [41].

Glasses have dielectric breakdown strengths two orders of magnitude higher than polycrystalline ceramics [1-5]. The presence of pores, grain boundaries and cracks make polycrystalline ceramics more susceptible than glasses to dielectric breakdown. These

sites act as field concentrators and will experience higher fields than the rest of the material. Partial discharges in those regions can erode the material, leading to degradation and finally contributing to total dielectric breakdown [3].

For defect free glass, the two main types of dielectric breakdown applicable to glass are thermal breakdown and avalanche breakdown. Thermal breakdown occurs as a result of the Joule heating produced from dielectric loss of the material. If the dielectric cannot dissipate heat fast enough there is a rapid increase in both conductivity and temperature until catastrophic failure occurs. [3, 5, 39].

Avalanche breakdown is more indicative of intrinsic breakdown strength. Free electrons in the conduction band of a dielectric can be accelerated in a high electric field. Conduction band electrons can be the result of electrons injection from the metal electrode or can already be present in very small concentrations. Energetic electrons are able to ionize other atoms in the material resulting in more electrons. The process continues until there are enough electrons present to force a rapid rise in conduction through the material. In glass, dielectric breakdown is catastrophic at the breakdown event and will physically crack or melt, preventing that spot from performing successfully as a dielectric [3, 5, 39, 41].

Many studies have been conducted to prevent complete device damage due to dielectric breakdown. By engineering electrodes that vaporize upon breakdown of the dielectric, the electrode material clears away from the breakdown event and that spot will not signal failure of the entire device. The concept of a vaporizing electrode material is called graceful failure or self healing [2, 13, 42].

For the reasons outlines above, it can be somewhat difficult to obtain the intrinsic value of dielectric breakdown strength for a material. Extrinsic factors that have an effect on dielectric breakdown strength are impurities or defects in a material, temperature of the sample when voltage is applied, humidity, electrode geometry, electrode material, duration of breakdown tests, frequency of applied field and sample thickness [3, 5]. Several investigators have explored the best conditions in which to measure the dielectric breakdown strength of several glasses. Some examples of their methods and what they observed are mentioned below.

Flowers [30] measured the dielectric breakdown strength of sealing glasses and other low melting temperature glasses for device passivation. His glass films were 5-15 microns thick and fabricated by suspending glass frit in an organic solvent, spin coating the substrate and sintering the films. Many of the compositions he looked at were lead aluminosilicates. In some cases he replaced lead with transition metal oxides. The highest dielectric breakdown strength glass turned out to be 20% SiO_2, 70% PbO and 10% Al_2O_3 with a dielectric breakdown strength of about 3 MV/cm. Some of the glasses he investigated had a dielectric breakdown strength as low as 0.4 MV/cm [30].

Von Hippel and R. J. Maurer measured the dielectric breakdown voltage of soda lime silicate glass over the temperature range -200˚ to 150˚ C. At low temperatures they observed the dielectric breakdown strength of the glass was about 5 MV/cm. They also compared the dielectric breakdown strength of silica versus crystalline quartz. At temperatures below 0˚ C silica has a dielectric breakdown strength 20-50% higher than crystalline quartz. As the temperature increase the dielectric breakdown strength of silica decreases and the dielectric breakdown strength of crystalline quartz increases to where it

is about 20% higher than silica. Overall, silica achieves a dielectric breakdown strength of about 7 MV/cm at -70˚C compared to quartz's 6.5 MV/cm at 70˚C. [17].

Austen and Whitehead looked at the behavior of silica and crystalline quartz and determined that the silica, with the same permittivity as crystalline quartz, had a higher electrical strength with a value of 5.4 MV/cm compared to 4.7 MV/cm. They also looked at a lead silicate glass and measured a dielectric breakdown strength between 5-6 MV/cm [15].

Vermeer did several exhaustive studies where he allowed one condition to vary while holding the rest constant. He looked at the dielectric breakdown strength of Pyrex, two additional sodium-containing glasses, and a boroaluminosilicate glass under varied temperatures, thicknesses and voltage ramp times. He also explored the difference surface treatments and electrode materials made on the dielectric breakdown strength. In the thermal breakdown regime, sodium content of the glass was correlated with low dielectric breakdown strength and high ionic conductivity [6-8]. He observed that the best conditions to measure intrinsic strength were with low temperatures, high ramp rates and thin samples. The glasses he studied had dielectric breakdown strengths ranging from 9 MV/cm to 11.5 MV/cm. The glass yielding the highest dielectric breakdown strength had the least sodium in its composition [6-8].

It was predicted by Frohlich that the dielectric breakdown strength of a material increases with decreasing thickness [16]. Thickness dependence has been experimentally verified in many studies of different materials [6, 13, 15, 16, 43]. The reason for this behavior is not fully understood. One theory is that a decrease in thickness will lead to a lower volume of defects. Studies have also looked at the effect of electrode area on

dielectric breakdown and found that larger electrode area will decrease dielectric breakdown strength [15, 44]. Since decreasing thickness or decreasing electrode area are both techniques that reduce the volume of material subjected to an electric field, the reduced electrode experiment results reinforce the idea that having a smaller volume of material will increase the dielectric breakdown strength. Another theory states that since thinner materials are better able to dissipate heat developed as a result of dielectric loss, the thermal breakdown regime is reduced.

CHAPTER 3

EXPERIMENTAL METHODS

3.1 THIN FILM SYNTHESIS

Alkali-free boroaluminosilicate glass films were fabricated by radio frequency magnetron sputter deposition. Films were deposited for several hours on 4-inch diameter 5-25 Ω cm bulk resistivity Nova Electronic Materials, Ltd. silicon wafers purchase with a 150 nm platinum/titanium coating. Bulk Schott AF45^{TM}, herein referred to as AF45, was used as the sputtering target materials. Platinum was used as the top electrode material.

The Kurt J. Lesker Company bonded 3-inch diameter AF45 glass targets, 200 microns and 400 microns thick. Some targets were bonded by submerging the glass and the copper backing plate in molten indium metal and applying pressure to attach the glass. The rest of the targets were bonded by using a sheet of elastomer between the glass and copper and applying pressure. The elastomer was cured and the excess was cut away from the edges of the target. Due to the brittleness of the glass and the pressure required to conduct the bonding, several pieces of glass were broken in the process. Bubbles were also trapped in many of the elastomer-bonded targets. A 100 micron thick piece of AF45 was bonded and used for sputtering but was too thin to withstand the process and broke when a bubble formed in the indium layer. Glass thicker than 400 microns has been bonded for use by previous students but cracked due to thermal shock.

A Kurt J. Lesker Co. CMS-18 magnetron sputtering system, shown schematically in Figure 3.1, was used to deposit the films. Two additional films were deposited, using

the same system model with additional features and a slightly altered geometry, by technicians at the Kurt J. Lesker Co. in Clairton, PA.

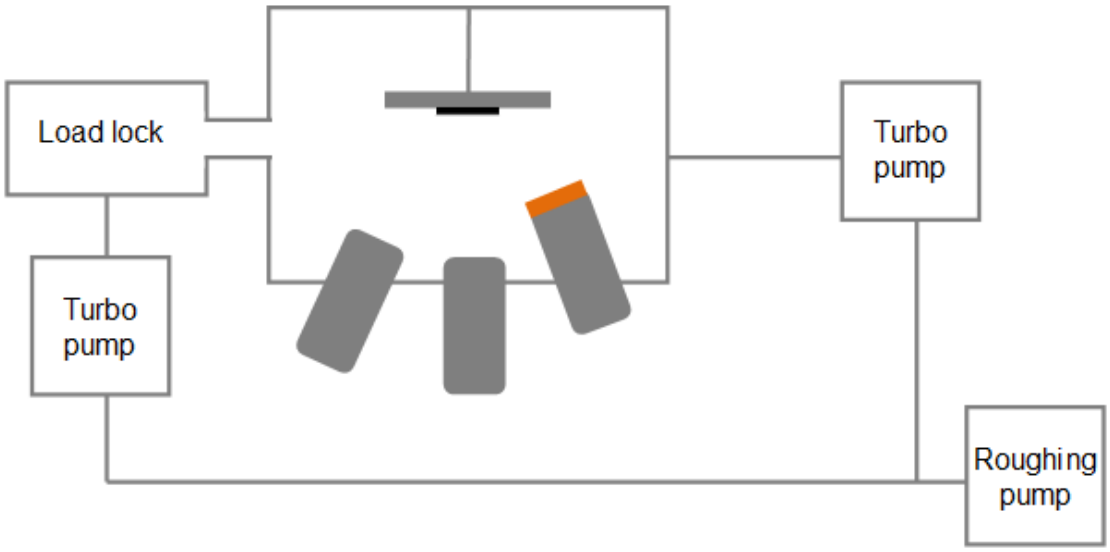

Figure 3.1: A diagram of a Kurt J. Lesker CMS-18 magnetron sputter deposition system. The system can run 3 different targets at once, two guns are radio frequency and one gun is direct current. The gun on the right is shown raised.

Primary deposition occurred at room temperature with an argon-to-oxygen ratio of 10:1 at pressure of 5 mtorr. Oxygen was added to the processing gas to better control the stoichiometry of the films. The large target-to-substrate distance in the processing chamber caused a significant portion of sputtered material to deposit on the walls of the chamber, further limiting deposition rate, and influenced the film uniformity across the substrate. The target-to-substrate distance was reduced to 10 cm from 20 cm, achievable by raising the target closer to the sample, shown in Figure 3.1.

An additional challenge imposed by the deposition tool was the absence of a deposition monitor. Often systems are equipped with a quartz crystal monitor to measure

deposition rate [24]. Without the addition of a deposition monitor, all thickness measurements were taken ex-situ.

The deposition chamber was coated with the target material for 30 minutes prior to film deposition to prevent contamination of the films by material sputtered by previous users. The substrates were not rotated to enhance the thickness gradient across the wafer during deposition in order to measure dielectric breakdown over a range of thicknesses on a single wafer. Figure 3.2 shows the thickness gradient that this deposition technique was able to achieve.

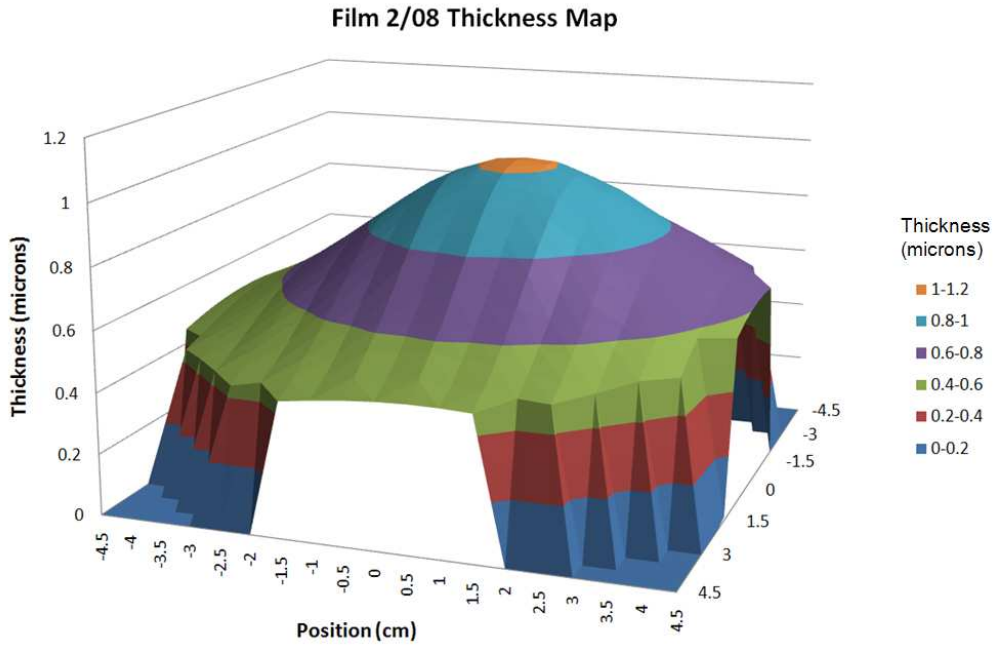

Figure 3.2: Thickness distribution of film 02/08 measured across a 4-inch wafer, achieved by the deposition technique described in Section 3.1.

The target power density during deposition was 1.95 W/cm^2 after ramping up the power at a rate of 10 watts every 10 minutes starting at 25 W and then increasing from 40

W to 90 W, to prevent thermal shock of the target. In order to achieve the shortest target-to-substrate distance for deposition the target gun was raised in the chamber.

Sputter conditions were developed by trial and error. The objective was to achieve the thickest films in a timely manner while maintaining the composition and thickness profile. Targets tended to crack when run above 90W but the deposition rate at that power was much less than an angstrom per second. A shorter target-to-substrate distance lead to an increase in deposition rate. The 5 mtorr deposition pressure was also determined to yield the highest deposition rate, pressures of 10, 15 and 20 mtorr were also evaluated.

Some samples were fabricated by the Kurt. J. Lesker Co. to explore the contributions of processing chamber geometry on the composition and thickness distribution of AF45 glass thin films. The target-to-substrate distance was 2.86 cm with a moveable target. The target was scanned from the center of the wafer to the outside while rotating the substrate at 50 rpm in order to achieve a uniform thickness. The process gas had an argon-to-oxygen ratio of 10:1 at a pressure of 4 mtorr. The target was run at 2.19 W/cm^2 after increasing the target power up from 0 to 100 W in 20 minutes. The target was cracked as a result of the rapid ramp rate. Two samples were fabricated on Si wafers without a continuous platinum electrode layer. Films will be referred to by the film designation in Table 3.1.

After thickness and optical property measurements, described in the next section, a 19 by 19 array of 3 mm diameter, 100 nm thick, platinum electrodes was deposited on top of the glass film using direct current magnetron sputter deposition through a 4-inch by 4-inch aluminum mask. Figure 3.3 shows a representation of a completed sample.

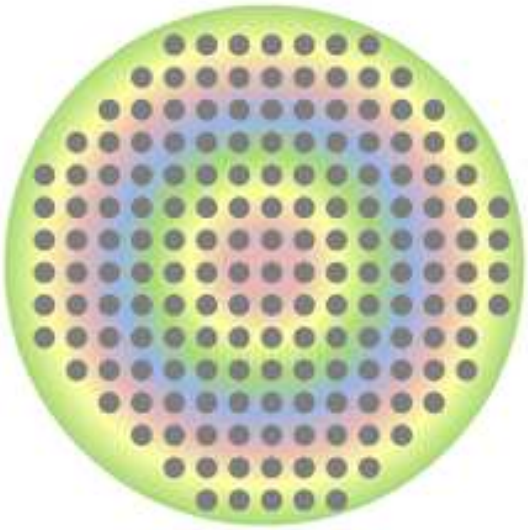

Figure 3.3: Representation of a thin film sample, top view, after deposition of glass and electrodes. The colors in the figure resemble the colors observed on the thin film due to light interference.

Table 3.1: Thin film sample designations.

Film Designation	Deposition Time (hrs)	Fabrication Location
09/18	24	Penn State
10/14	30	Penn State
11/18	36	Penn State
11/05	18	Penn State
12/08	6	Penn State
12/09	12	Penn State
12/10	12	Penn State
02/08	10	Penn State
L1	3.25	Kurt J. Lesker Co.
L2	6.75	Kurt J. Lesker Co.

A section of film 12/10 was annealed at 663˚C for about 15 minutes. The entire furnace ramp time and hold time was about two hours. The sample was allowed to air cool with the furnace.

A film was also deposited for 8 hours on a flat strip of Kapton in order to qualitatively determine the type of stress present in the films. It was observed that the films exhibit some degree of compressive stress. Stresses in thin films are common and result from the non-equilibrium nature of deposition [45].

3.2 COMPOSITIONAL ANALYSIS

Primary compositional analysis of the films was preformed using x-ray photoelectron spectroscopy (XPS) using a Kratos Analytical Axis Ultra XPS with a monochromatic Al kα source. Samples were taken from the center and edge of each wafer in order to determine if a compositional gradient was present across the diameter of the film. XPS was conducted on some samples after dielectric breakdown testing and cleaning, described later in the chapter, and some were measured but were not tested. CasaXPS was used in data analysis.

A 20 eV pass energy was used during high resolution scans and an 80 eV pass energy was used during survey scans. A charge neutralizer gun was used to prevent charging of the samples during analysis. Quantification was preformed using high-resolution scan windows.

In order to quantify the composition and compare spectra, all peaks were shifted so that the full width half max (FWHM) of the C1s peak was located at 285 eV. Peaks were fit with the standard procedure for CasaXPS using a linear background. The exception to standard procedure involved measuring the area under the B 1s peak.

The Ba 4p 1/2 peak, FWHM at a binding energy of 193 eV, overlaps the B 1s peak, FWHM at a binding energy of 189 eV. In order to deconvolute the peaks, they were fit using the following assumptions: the FWHM of Ba 4p 3/2 and Ba 4p 1/2 is equal and the separation distance between the Ba peaks is fixed at 14 eV. A boron-free barium containing glass was used as a reference to determine the area and dimensional relationship between the Ba peaks in a similar glassy matrix. The 2 Ba peaks, B 1s peak and 3 fine structure peaks [46] were fit empirically until the best match was determined.

In addition to the peak overlaps previously mentioned, the Ba peaks are distorted by the inelastic background for the Si 2s peak. A Shirley background was used to fit the Si loss peak region, center region of Figure 3.5, and 3 peaks were fit under the curve and constrained to the Si 2s peak in a silica standard spectrum. By fitting these peaks the area contribution was removed and the true Ba 4p 1/2 peak was measured. Figure 3.5 shows the regions and peaks previously described.

The effect of adventitious carbon was normalized out of the total composition using the procedure outline in G. Smith’s publication [47].

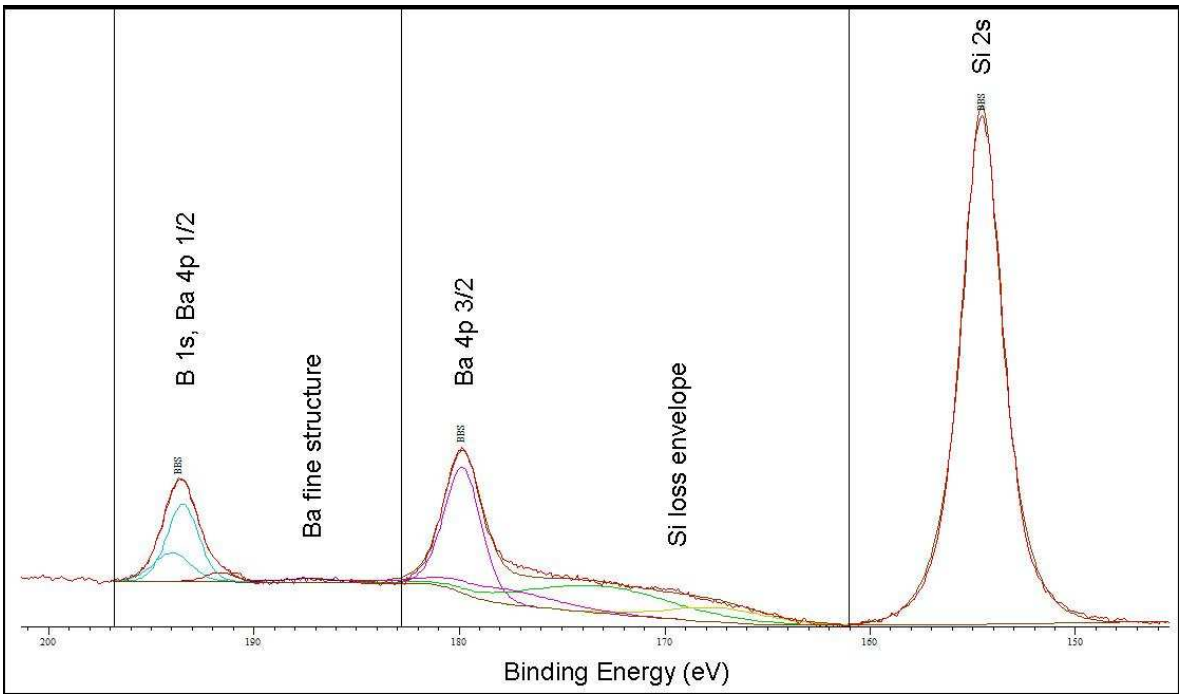

Figure 3.4: Casa XPS regions and components needed to fit the B 1s peak. Spectrum was taken from a bulk AF45 vacuum fracture surface.

Additional compositional analysis was performed using electron probe microanalysis (EPMA) on a piece of film 11/18 taken from the center of the 4-inch wafer. A Cameca Model SX-50 was operated at 10 KeV and 20 nA with a 20 micron spot size. The standards used were AF45 bulk glass, NIST uncertified glass K919 and the minerals Albite, Benetoite and Apatite. Measurement and analysis was preformed by Materials Characterization Lab (MCL) Technician Mark Angelone.

3.3 OPTICAL SPECTROSCOPY

A combination of dual rotating compensator multichannel ellipsometry [48] (J. A. Woollam Company Inc. model RC-2 spectroscopic ellipsometer) and spectroscopic

reflectometry (n&k Analyzer 1500) was used to measure the optical constants and map the thickness of the films as a function of position on the wafer surface. Since having a detailed thickness profile of the samples was very important to the calculation of field strength, many spots had to be analyzed. Reflectometry was used to supplement ellipsometry because of the mapping capabilities of the reflectometry tool.

The reflectometer was equipped with a stepper stage that allowed several hundred spots in a periodic array to be measured very quickly. It would be impractical to measure the same number of spots with a stationary stage. The user would have to manually move the sample between each measurement and would not be able to maintain the well-defined pattern of spots allowable by using the reflectometer.

Ellipsometry measures Δ and Ψ for a material whereas reflectometry measures the difference in intensity between the beam before and after it has reflected from the sample. Δ is the change in polarization when light is reflected from a surface, denoted by Equation 3.1, where δ_1 is the phase difference between the parallel (p) and perpendicular (s) waves before reflection and δ_2 is the phase differences after reflection. Ψ measures the relationship, denoted by Equation 3.2, between the magnitude of the Fresnel reflection coefficients of the parallel and perpendicular waves [49].

$$\Delta = \delta_1 - \delta_2 \qquad [3.1]$$

$$\Psi = \mathrm{Tan}^{-1}\left[|r^p|/|r^s|\right] \qquad [3.2]$$

Film 11/05 was measured by spectroscopic ellipsometry at 16 spots across the thickness gradient using an angle of incidence of 70° over a spectral range from 240-1700

nm. Several other samples were measured at select spots and compared to the ellipsometric date of film 11/05 to verify that film 11/05 was a good representation for all films sputtered under the same conditions.

In order for the best fit, a 5 medium structural model, shown in Figure 3.6, was used to represent the thin film. The topmost layer represented the surface roughness and the thickness non-uniformity of the film by modeling the air-glass interface. The second layer represents the optical properties of the bulk film. The layer closest to the platinum substrate represented the interface between the glass and platinum. The silicon substrate was not included since the platinum layer was optically opaque such that light was not able to transmit through and reflect form the platinum/silicon interface.

The two interface layers were represented as 0.5-0.5 Bruggerman effective medium approximations (EMA). An EMA takes into account the interface between two layers as a combination of their optical properties and helps to improve the fit of the model to the measured spectra of the film [49, 50].

The bulk layer was modeled as a Sellmeier oscillator with an absorption coefficient equaling zero within the data collection range. A Sellmeier oscillator is often used for dielectric materials where the absorption of light occurs outside of the spectral range [51]. In the case of a silicate glass, it begins to absorb above about 2500 nm and below about 100 nm [29].

Optical dispersion curves were generated for each point based on the ellipsometry measurements. Each refractive index value along the curve was averaged with the 15 other points corresponding to the same wavelength to generate an average optical

dispersion curve. Since the standard deviation of any one point was less than 0.009, the average curve was used to represent the films.

Figure 3.5: A five medium structural model used to represent the glass thin films during modeling of thickness and optical properties.

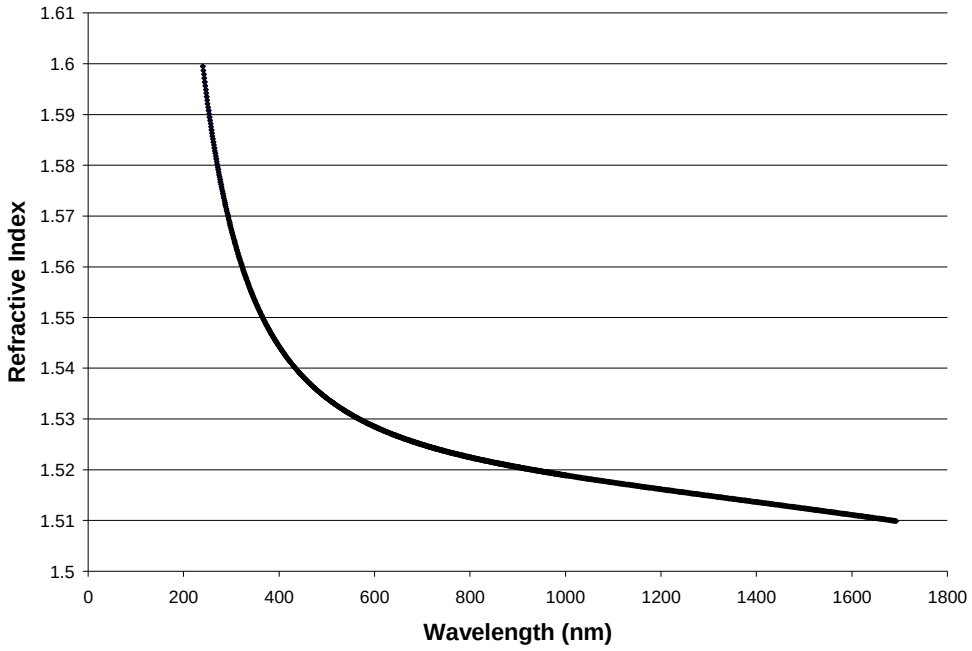

Figure 3.6: Average optical dispersion curve for AF45 thin films on platinum generated with ellipsometry measurements and modeling. This information was programmed into the reflectometry analysis software.

The average optical dispersion data of the bulk film, shown in Figure 3.6, the EMA for the glass-surface and glass-platinum interfaces was programmed into to the n&k analyzer data analysis software.

A 19 by 19 array with a 0.5 cm distance between spots was measured with the reflectometer over a spectral range of 190-1000 nm at a near-normal incident angle of 5˚ on all samples before the top electrodes was deposited. A 30 by 30 array with a 0.3 cm distance between spots was used for films that had electrodes deposited on the surface prior to mapping. In the thickness map for these samples erroneous data due to the different optical properties of the platinum electrodes was removed. The thickness values of those spots were approximated by using the average thickness value of the 8 surrounding spots.

The thicknesses measured by the ellipsometer were compared to the thickness measured with reflectometry to determine if there is significant variability due to averaging of the dispersion data. The dispersion curves representing the highest and lowest refractive index spots were programmed in the n&k analyzer software. The thickness difference was compared to that taken with the average dispersion curve to determine error in measurement. The thickness difference varied for every spot measured on the sample, but the values were only 1-2% different from the average thickness.

A Bruker IFS 66/S Fourier Transform Infrared (FTIR) Spectrometer in combination with a Hyperion 3000 Microscope was used to perform FTIR spectroscopy on the thin films. Absorbance measurements were taken with attenuated total reflection (ATR) to compare bulk glass with glass thin films on platinum. ATR was chosen in order to have comparable spectra between the film and the bulk glass since in reflection the

film exhibits reflection-absorption while the bulk glass exhibits reflection. The mixed nature of the thin film spectra makes comparison difficult because it contributes to the peak shift relative to the bulk spectrum.

3.4 PROFILOMETRY AND MICROSCOPY

In order to determine the root-mean-square (RMS) roughness, films were measured using a Wyko NT1100 Optical Profilometer. The tool was operated in phase-shift interferometry (PSI) high magnification mode with a 20X objective. Several spots were taken on each sample and each measurement was taken 3 times and averaged.

A tilt correction in the software was applied to the data removing the effect of the tilt stage from the roughness profile of the film and the bulk glass. A cylindrical correction was also applied to the bulk glass to remove the effect of the slight bowing that occurs when the glass sits on the sample stage of the optical profilometer.

An Olympus B60 optical microscope equipped with a PAXcam was used to capture images of breakdown spots. Images were taken at 5X and 20X magnification in bright field.

A JEOL 69090F field emission scanning electron microscope (FE-SEM) was used to capture images of the film surface and cross section in order to characterize observable microstructure or visible damage as a result of dielectric breakdown testing and to verify film thickness. Films were observed before and after being tested. Tested samples were cleaned (using the method outline later) before observation. All samples were diced and

coated with a 20 Å layer of iridium to reduce charging. Samples were mounted with minimal carbon tape and silver paste.

One sample was measured at a 20˚ glancing angle to look for surface texture and microstructure. Figure 3.8 illustrates the sample configuration.

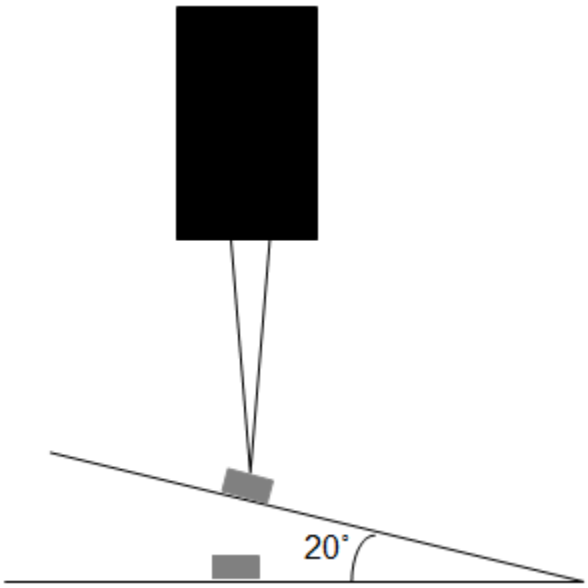

Figure 3.7: Illustration of how the surface of a thin film is measured at a glancing angle in FE-SEM.

3.5 DIELECTRIC BREAKDOWN TESTING

The samples were submerged in a dielectric fluid, Galden HT-200, and connected to a Trek Model 30/20 30kV-max DC high voltage source. Measurements were taken using LabVIEW software.

The testing setup can be observed in Figure 3.8 and is described schematically in Figure 3.9. The stainless steel probe was placed in contact with the center of the top

electrodes and connected to ground. The sample is pressed firmly to a copper plate which acted as the anode. Voltage was increased at a rate of 250 V/s until conduction occurred. All tested spots on select films were tested a second time. The probe was placed on the electrode where there was no visible damage or clearing away of the electrode material.

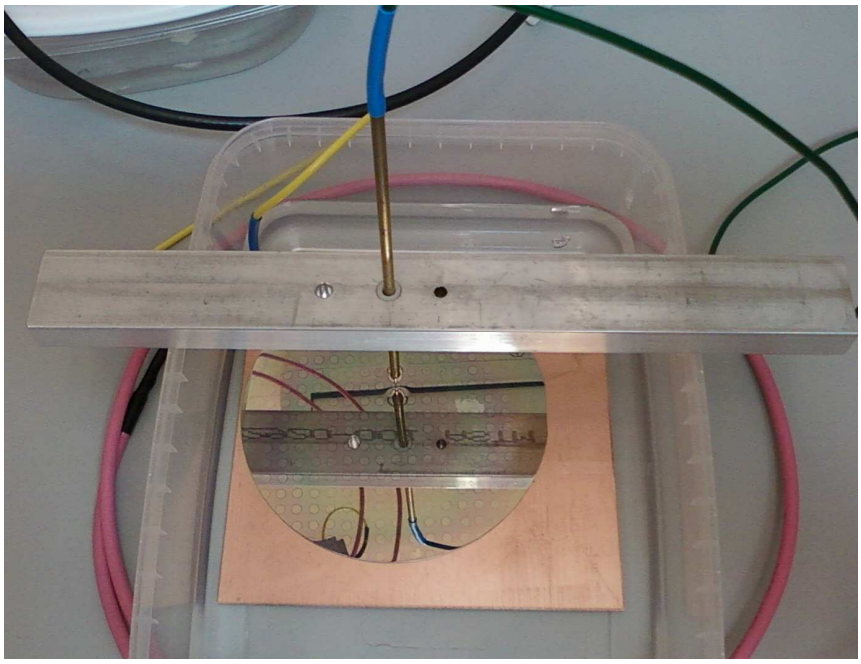

Figure 3.8: Photograph of the dielectric breakdown test configuration with thin film sample. The copper plate is the anode and the steel probe is the cathode.

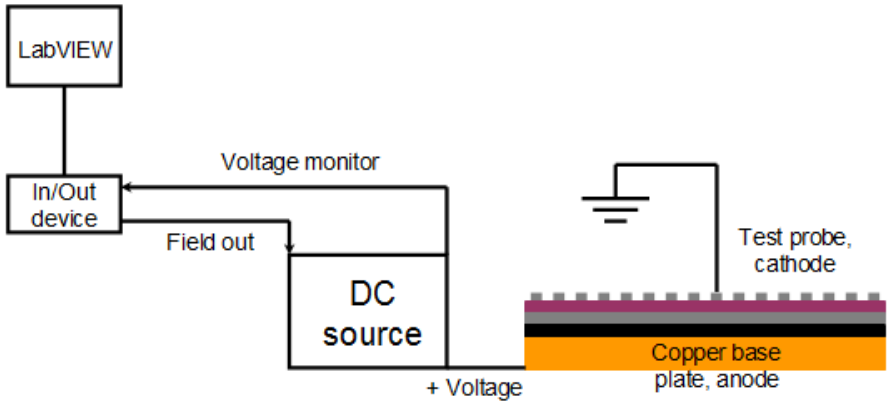

Figure 3.9: Schematic of the dielectric breakdown test configuration with thin film sample.

After dielectric breakdown testing was completed, samples were cleaned using the following procedure:

- Rinsed with Fomblin PFS-2 dielectric fluid
- Submersion in acetone for 10 and 15 minutes in an ultrasonicator, rinsing container and using fresh acetone each time
- Submersion in ethanol for 10, 20 and 30 minutes in an ultrasonicator, rinsing container and using fresh ethanol each time
- Blown dry with dry nitrogen

CHAPTER 4

RESULTS AND DISCUSSION

The glass thin films in this study were deposited by radio frequency magnetron sputter deposition under identical power and pressure conditions. Each film was deposited for a different amount of time and without the use of rotation, to enhance the range of thicknesses across the substrate.

The films were characterized in order to understand their dielectric properties and how they related to the bulk glass. The properties of the films and the bulk glass are compared and related to dielectric breakdown strengths measured for each set of samples.

4.1 THIN FILM CHARACTERIZATION

4.1.1 Microstructure

Figure 4.1 shows a cross section taken with FE-SEM of film 12/10. The top layer is the glass film, the lighter layer in the middle is the continuous platinum layer and the layer on the bottom exhibiting fracture lines, due to dicing, is the Si substrate. The glass film has a dense and uniform microstructure.

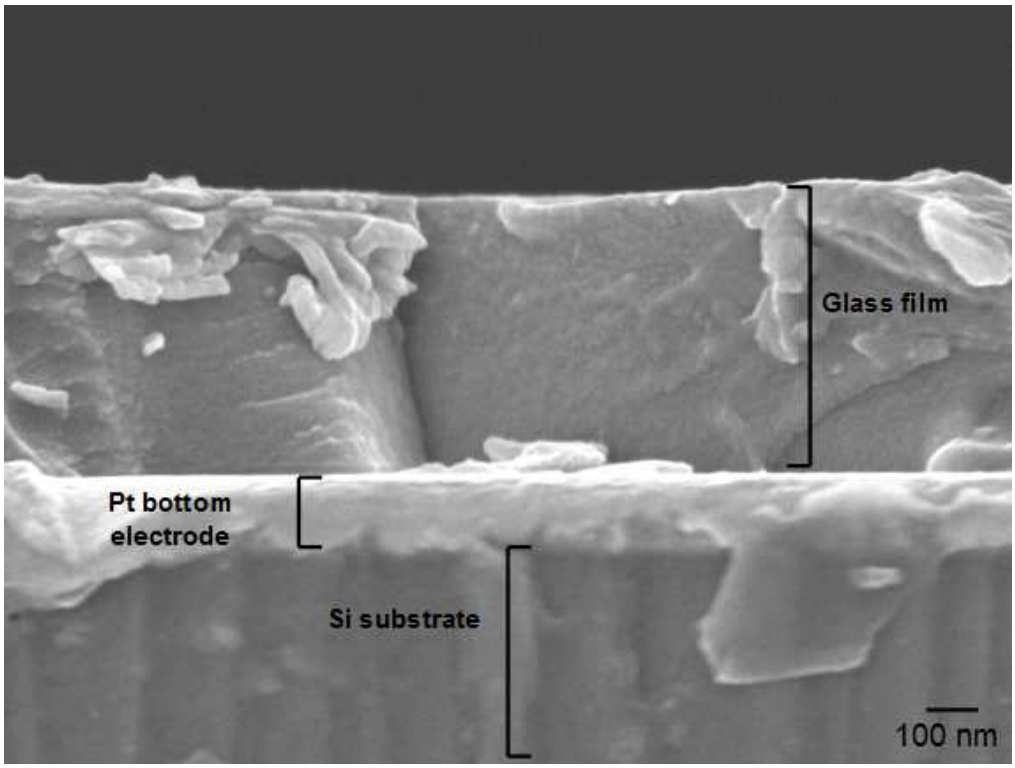

Figure 4.1: Field emission scanning electron microscopy image of film 12/10 in cross section. The top layer is glass, the light layer in the center is platinum and the bottom layer is the silicon substrate.

Based on previous thin film studies, columnar structures are usually formed when deposition occurs at room temperature. The modified zone model of thin film growth structure predicts the microstructure of thin films based on the ratio of substrate temperature to melting temperature of the material and the pressure which deposition occurs [52]. Since no substrate heating was applied, the substrate temperature was estimated to be between room temperature and 100˚C and the glass transition temperature, 662˚C, reported by Schott, was used in place of the melting temperature. Based on the ratio calculated and a deposition pressure of 5 mtorr, the films would be expected to exhibit densely pack fibrous grains in transition to columnar grains.

Figure 4.2 illustrates the surface of the film in two images of the same spot at the same magnification. Figure 4.2 b) was taken at a glancing angle while the sample stage was tilted 20˚ with respect to its load position. The incident view of the films shows no detectable surface structure. The glancing angle shows some degree of surface roughness. There appear to be 20 nm diameter features on the surface. The surface roughness of the films on a larger scale was measured using optical profilometry.

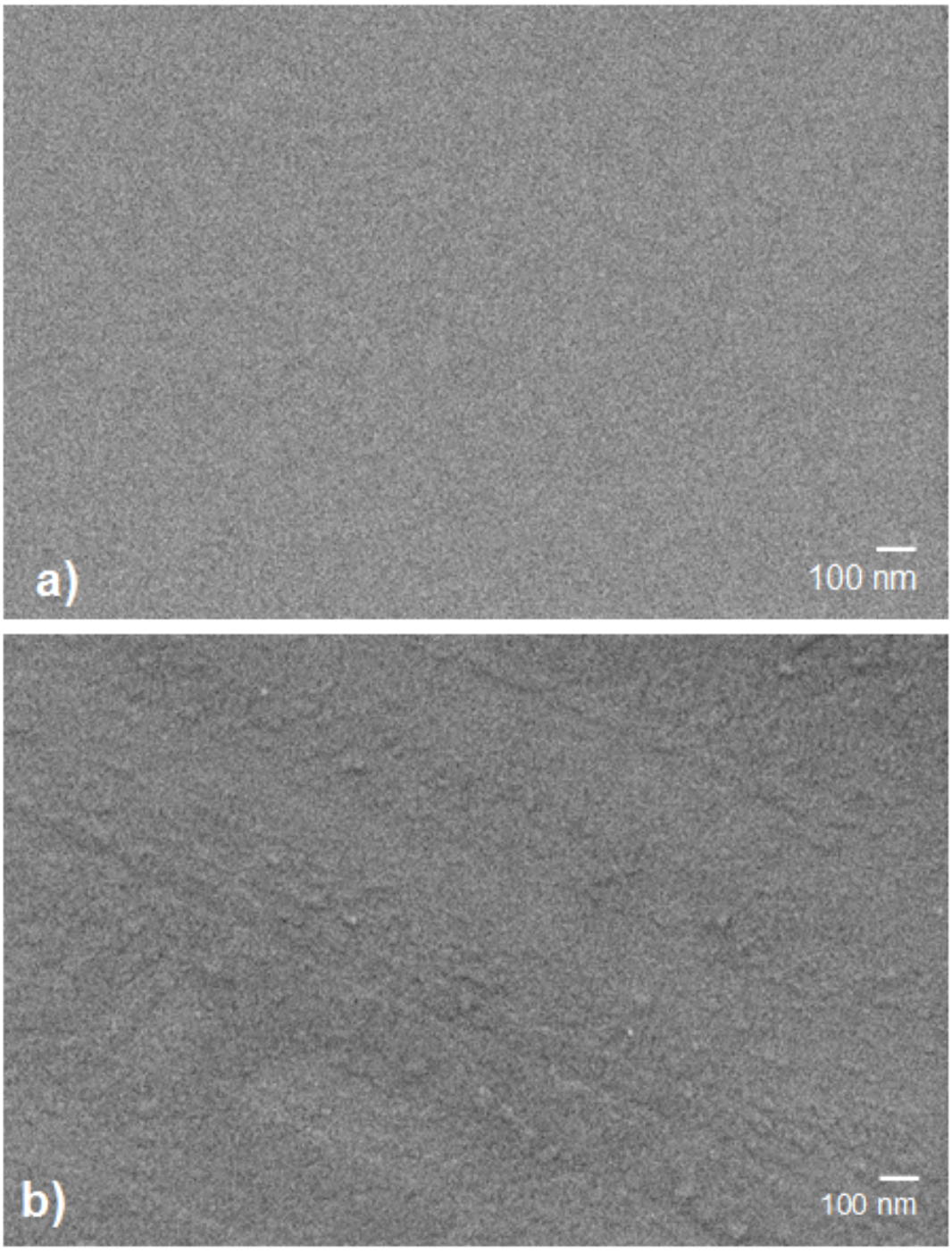

Figure 4.2: a) FE-SEM image of the surface of film 12/10 at an angle of 90˚. B) FE-SEM image of the same spot at an angle of 20˚ which highlights some surface roughness. Both images were taken at the same magnification.

Table 4.1 presents the average root mean squared (RMS) roughness calculated from 3 spots on each of 6 glass thin films, 4 pieces of bulk glass and 3 pieces of etched glass. Figure 4.3 shows a spot measured to have a roughness representative of the average total film roughness, 0.66 ± 0.15 nm. The film appears to have some topography in addition to a slight roughness.

Table 4.1: Average RMS roughness (nm) of the surfaces of as received bulk AF45, etched bulk AF45 and several thin films.

Sample	Film						Bulk	
	9/18	10/14	11/05	11/18	12/08	12/10	As received	HF etched
Ave RMS Roughness (nm)	0.66 ± 0.06	0.60 ± 0.07	0.67 ± 0.13	0.88 ± 0.12	0.48 ± 0.09	0.67 ± 0.13	0.30 ± 0.09	0.66 ± 0.37

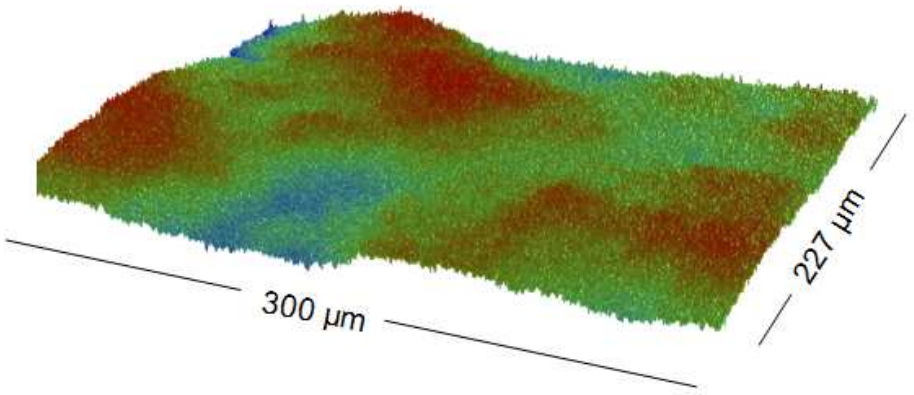

Figure 4.3: Surface profile taken from film 10/14 approximately representing the average roughness value. The RMS roughness in the figure is 0.67 nm.

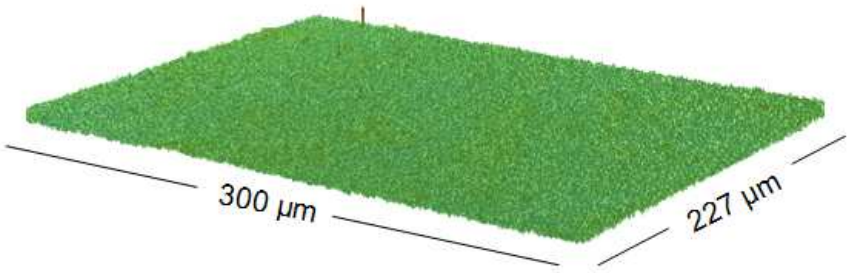

Figure 4.4: Surface profile taken from a 46.8 micron thick piece of as received AF45 having the average roughness value, 0.30 nm.

Figure 4.4 shows a spot taken from the as received bulk AF45 glass (~50 um thick). The surface is very smooth and uniform. After etching in 5vol% HF for 1, 5, and 10 minutes the RMS roughness of bulk AF45 increased by a factor of 2. Figure 4.5 represents a spot close to the average roughness of the etched bulk glass. The change in height for the film is around 4 nm whereas the etched film has a change around 3 nm.

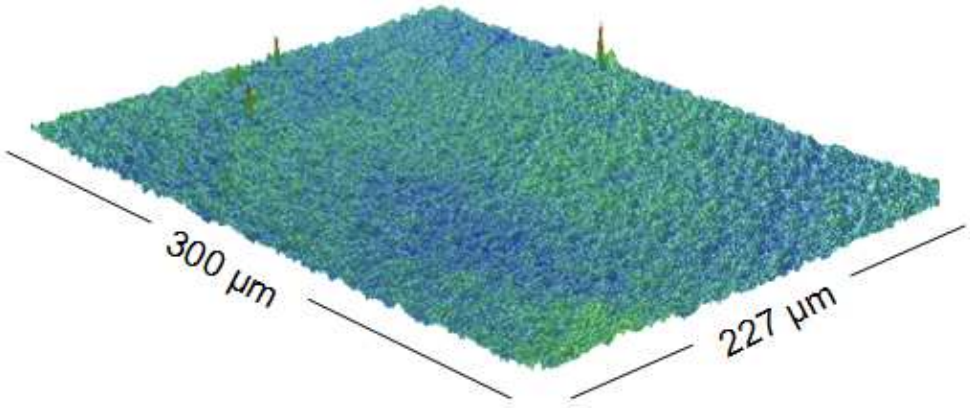

Figure 4.5: Surface profile taken from a piece of AF45 etched in 5% HF for 5 minutes. The sample shown has an initial thickness of 46.5 microns and a final thickness of 34.1 microns. This sample was chosen to represent the average roughness value of etched AF45. The RMS roughness in the figure is 0.65 nm.

The RMS roughness measured on the glass samples used in the Lee study is higher than the roughness presented above [13]. In order to compare the roughness values for the bulk glass measured by Lee and the films, the ratio of RMS roughness (nm) to thickness (nm), multiplied by 10,000 (for ease of comparison), was calculated. It seems that the ratios for bulk and thin films are relatively close to one another. The bulk glass ratio values ranged from 1.5-6.5. All of the films measured fell into that range with the exception of the two thinnest samples.

While the RMS roughness of the thin films is similar to that of the etched glass, the surface does not appear as flat. During deposition, the substrate is bombarded with target atoms. The atoms can undergo several processes, depending on ion energy, when they come in contact with the surface. Once they become part of the film they may or may not have enough energy to diffuse to a more energetically favorable position. In contrast, melt processing of glass allows for a smooth pristine surface.

An aspect that is unique to thin film deposition is the potential thickness gradient that can be achieved. Figures 4.6 and 4.7 present the thickness data taken from film 11/18 as a representative example of the thickness profile of the films fabricated during this study. The film has a dome shape, where thickness is greatest in the center of the wafer and decreases as it approaches the wafer edges, by design of the deposition conditions. All films fabricated at Penn State were measured and observed to have the same general shape but vary in thickness. The thickness profiles of the other films can be observed in the appendix.

Figures 4.8 and 4.9 represent the films deposited at the Kurt J. Lesker Company. These films were not deposited to have an intentional thickness gradient.

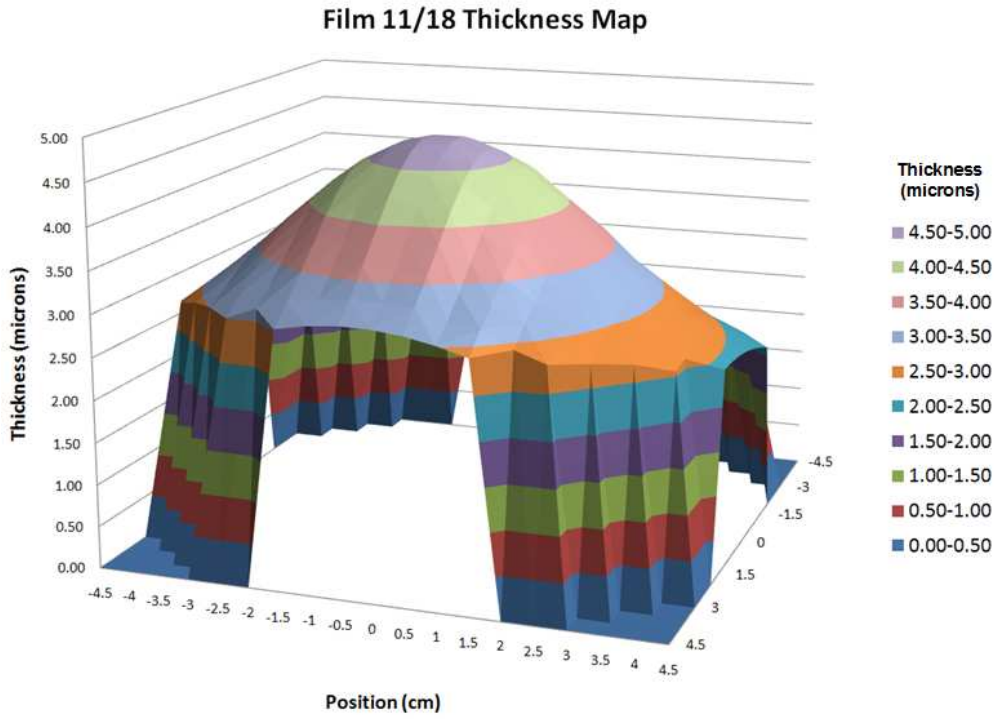

Figure 4.6: Thickness map of film 11/18 showing a 3D view of the thickness distribution.

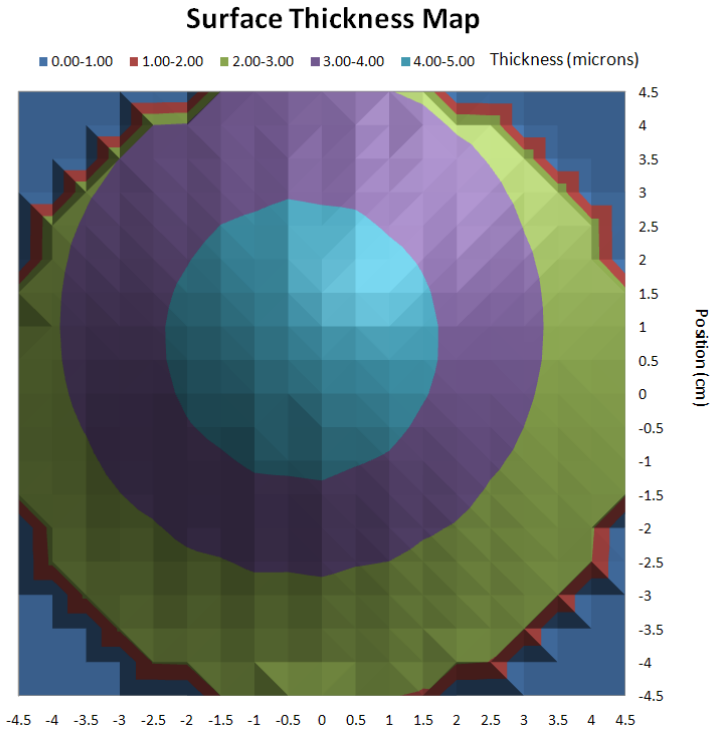

Figure 4.7: Thickness map of film 11/18 showing the top view of the sample.

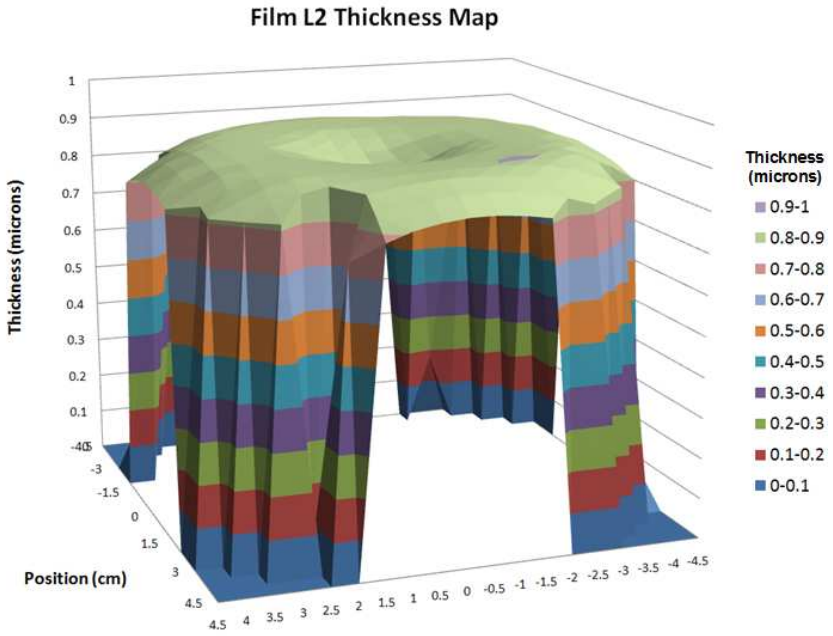

Figure 4.8: Thickness map of film L2 showing a 3D view of the thickness distribution.

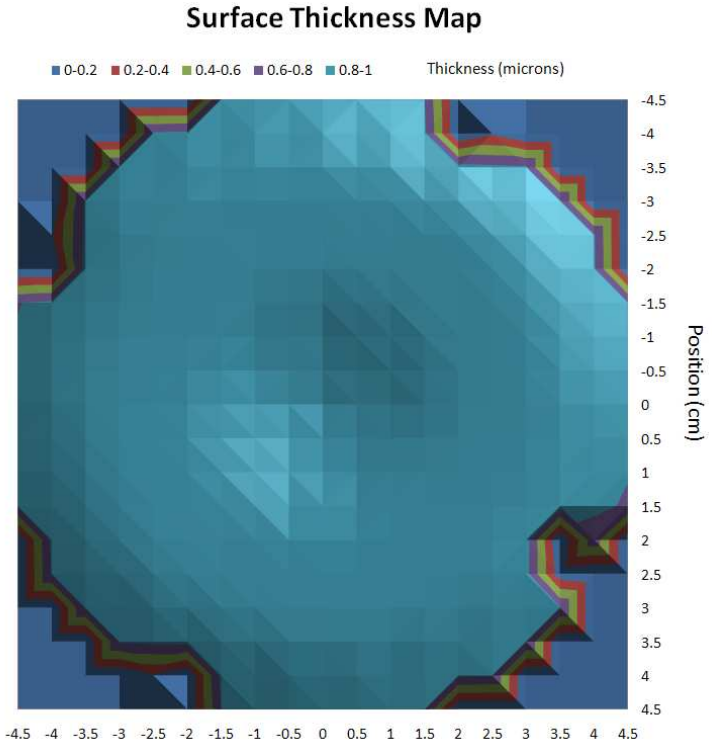

Figure 4.9: Thickness map of film L2 showing the top view of the sample.

Thickness distribution is an aspect of sputter deposition that depends on a large number of factors. There is a simple assumption based on the cosine law applied to vacuum evaporation to predict the thickness gradient of a film. Knowing the dimensions of the deposition system can help estimate the potential thickness gradient. Equation 4.1 where d_0 is the thickness in the center of the substrate, d is the thickness at l, S is the radius of the magnetron race trace on the target and h is the target-to-substrate distanced [22]. The shape of the films agrees with the thickness gradient predicted by this equation.

$$\frac{d}{d_0} = [1 + (S/h)^2]^2 \quad \frac{1 + (l/h)^2 + (S/h)^2}{\{[1 - (l/h)^2 + (S/h)^2] + 4(l/h)^2\}^{3/2}} \qquad [4.1]$$

This simple equation cannot be applied to the films fabricated at the Kurt J. Lesker Company because of the complex process they used to fabricate films. Their process involved moving the target with respect to the substrate. Equation 4.1 deals with a stationary magnetron target parallel to the substrate.

4.1.2 Composition

In Table 4.2, the composition of the films measured before breakdown testing and after breakdown testing are displayed along with bulk AF45 compositions. A ‘C’ or ‘E’ by the film name denotes center and edge respectively, describing at what location the samples were taken from on the 4-inch wafer. In the case of the films fabricated at Penn

State, ‘C’ samples are thicker than ‘E’ samples by about 20%. For the films fabricated at the Kurt J. Lesker Company, ‘C’ samples are thinner than ‘E’ samples by about 6%.

Film 11/18 has a number of impurities that the other films do not exhibit because it was measured after being submerged in the dielectric fluid. It is included in the discussion in order to compare the composition of the film measured by XPS and EPMA. Other post breakdown test samples were also measured with XPS; the compositions are available in the appendix. Figure 4.10 shows that the XPS spectrum for a bulk AF45 vacuum fracture surface and for film 12/10 differ compositionally.

Table 4.2: Compositions taken by XPS and EPMA of several films fabricated at Penn State and at the Kurt. J. Lesker Company. Bulk glass values are also included for comparison.

Film	Characterization Method	Mol %					Impurities
		SiO_2	B_2O_3	BaO	Al_2O_3	As_2O_3	
Bulk	EPMA	63.9	15.0	11.7	9.1	0.2	C, Na
Bulk	High res XPS vacuum fracture	64.8	11.5	14.8	8.9	0.3	C, F
L2C	High res XPS	76.7	10.9	3.8	8.6	0	C, Ar, F, N
L2E	High res XPS	80.8	6.3	5.2	7.7	0	C, Ar
12/10C	High res XPS	71.3	15.8	2.9	9.8	0.3	C, N
12/10E	High res XPS	72.6	12.2	4.9	10.0	0.3	C, N
11/18C	EPMA	60.8	20.8	7.0	11.2	0.2	C, Ar
11/18C	High res XPS	72.5	15.3	2.9	9.0	0.2	C, Mg, Na, Cu, F, Ca, K, Pt

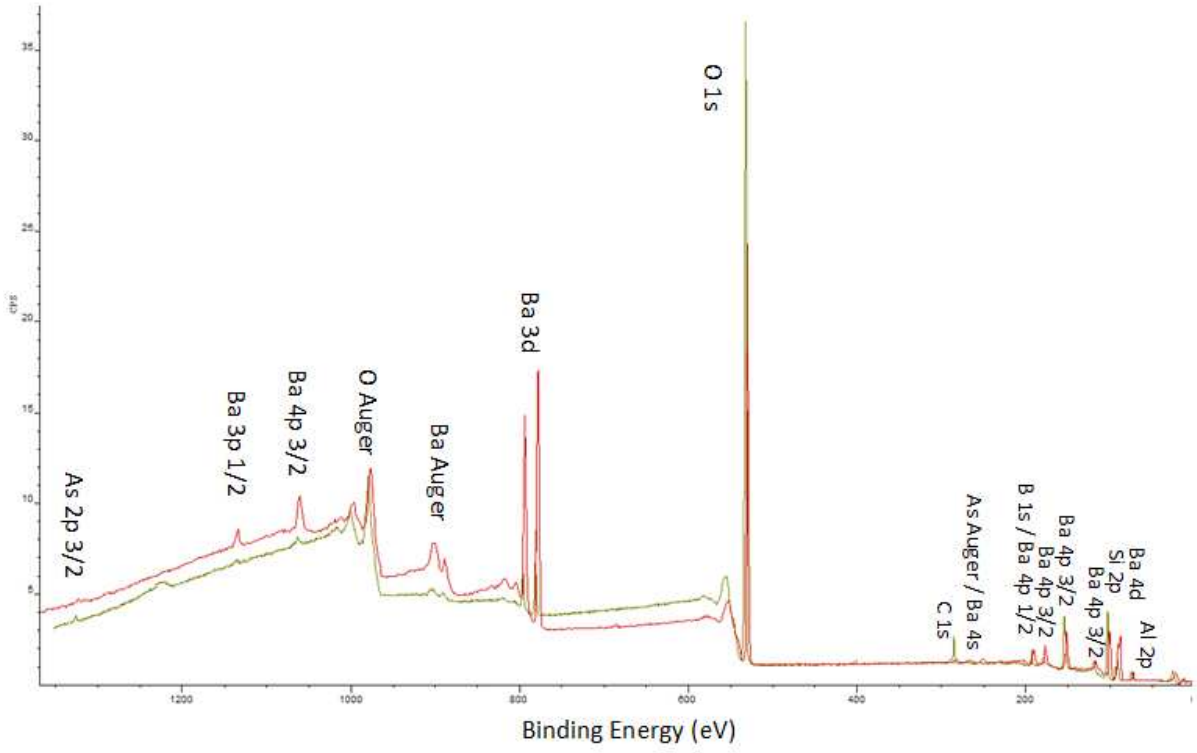

Figure 4.10: XPS survey scan comparison of a bulk AF45 vacuum fracture surface (red) and film 12/10 (green).

The composition of the deposited AF45 thin films was found to differ from that of bulk AF45. All of the films are more silica rich with respect to the bulk due to the depletion of B and Ba during deposition. The composition of the films based on the location on the wafer also differs. Table 4.3 shows the percent differences in composition of the films versus the bulk and of the films versus the alternate spot on the wafer.

Table 4.3: Percent difference of the film spots with each other and of the films compared to bulk AF45.

Percent Difference Within Each Film					
Film	SiO_2	B_2O_3	BaO	Al_2O_3	As_2O_3
Lesker	5.2	54.6	31.9	9.81	0
12/10	1.7	25.6	53.4	2.05	24.0
Percent Difference Between Film and Bulk					
Lesker	22.4	42.4	61.2	9.4	100
12/10	11.8	6.3	66.4	10.4	4.45

Film 12/10 is more compositionally consistent than the film deposited at the Kurt J. Lesker Company with the exception of BaO content. For both films, boron is more abundant in the center and barium is more abundance at the edges. Since larger atoms have been observed to sputter from the target at oblique angles, and small atoms at an angle close to the incident angle of bombardment, [26] the barium would have been expected to exhibit a more uniform distribution with a smaller rather then larger target-to-substrate distance. The Lesker system has a throw distance of 2.86 cm whereas the Penn State system has a throw distance of 10.16 cm. It also makes sense that since the target is bombarded at about a 90˚ incident angle, the light atoms would be more abundant in the center and the heavier atoms more abundant near the edges.

The other significant difference in both films is the B_2O_3 composition. B_2O_3 is also known for its increased volatility [32] and is therefore more prone to be depleted during deposition. According to XPS analysis some films exhibited a slight oxygen deficiency, from 0-5% deficient. It is common for oxygen to be deficient in sputter deposited oxide films and is the reason for adding oxygen to the process gas [35, 53].

EPMA was preformed on sample 11/18 to clarify the composition of barium and boron in the sample since the Ba 4p 1/2 peak overlapped the B 1s peak on the XPS spectra. In Table 4.2 the two entries for film 11/18 C do not report similar compositional data. Since both samples were taken from the same region of the sample they should exhibit similar compositions. The EPMA measured silica content and BaO content are closer to that of the bulk than the film. The boron detected by EPMA seems erroneous which may be due to the low sensitivity of the technique to the lighter elements.

The difference in sampling depth of the techniques and the surface contamination may affect the composition measured. XPS sampling depth is on the order of nanometers and the surface of the film was contaminated by the dielectric fluid. The sampling depth of EPMA is on the order of microns, very close to the thickness of the film. Only the thickest sample was tested in order to avoid influence of the substrate in the measurement. The differences in composition may also suggest that the composition of films vary with thickness. There is close agreement in composition of EPMA and XPS preformed on bulk glass. The bulk glass is more uniform and much thicker than the sampling depth of EPMA, reinforcing the previous conclusions taken from the thin film discussion.

4.1.3 Structure

FTIR is often used to compare structural and compositional differences between materials. Figure 4.11 compares two spectra taken with ATR of the bulk spectrum (in red) and the film spectrum (in blue).

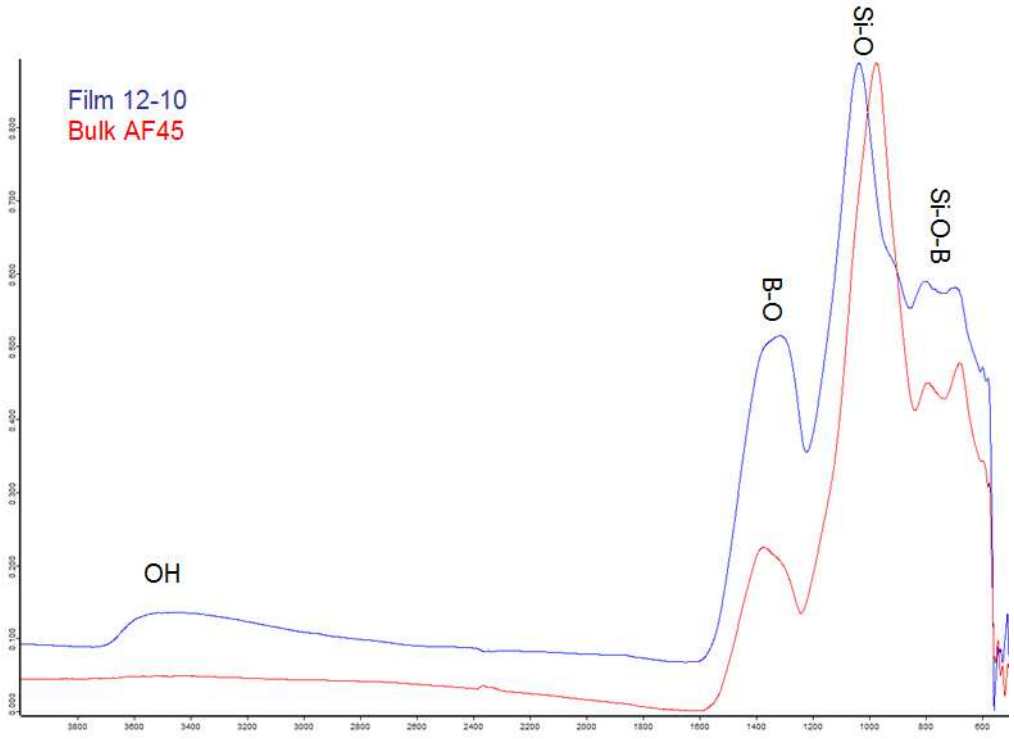

Figure 4.11: FTIR spectra taken with ATR of bulk AF45 (red) and film 12/10 (blue).

It is apparent that there are differences between the film and bulk spectra. Compositional differences and a difference in density will cause peaks to shift. A refractive index change will also cause peak shifts but can be related to composition and density. Referring to the results of XPS, the films do exhibit differences in composition compared to the bulk. In addition to a difference in composition, it is common for films to be less dense than their target material, especially when no substrate heating was used during deposition or if the films were not annealed [54].

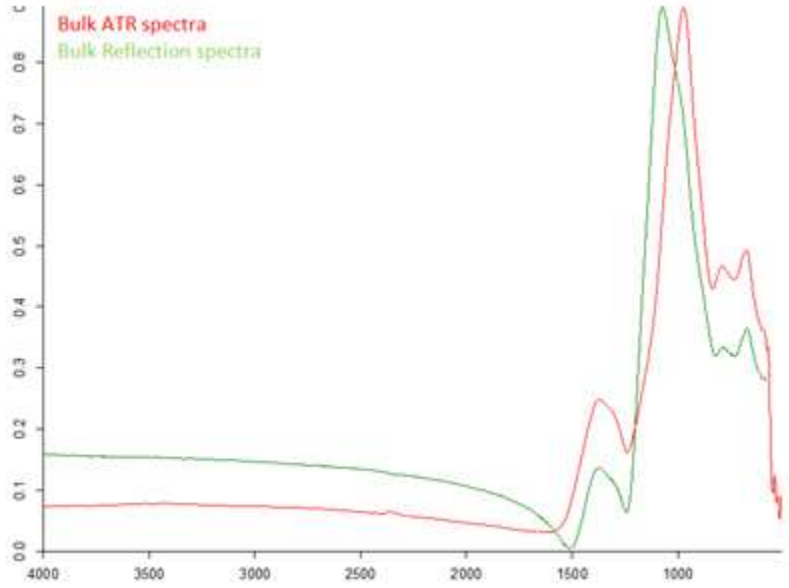

Figure 4.12: FTIR spectra taken with ATR and reflectance of bulk AF45 showing the difference in peak location and shape depending on the measurement technique.

Peaks do not reside in the same location for spectra taken with ATR and spectra taken in reflection as is demonstrated by Figure 4.12. For this reason, the ATR vibrational spectra in Figure 4.11 will be used for a qualitative comparison of the film and the bulk glass.

At 3600 cm^{-1} the film has a peak due to OH vibrations (associated with molecular water), that the bulk does not. This indicates that there is water as an impurity in the film, or that the film is more prone to water adsorption. It is also possible for water to enter the structure of the glass as a silanol (SiOH), although direct evidence is not apparent in the spectra. The presence of water (molecular or structural) can significantly affect the breakdown strength of a dielectric by acting as a charge carrier, or by altering the properties of the glass. In silica there is a slight increase in density and refractive index as a result of 1000 wtppm of water [55].

The presence of water could be due to contamination in the processing chamber. Though the base pressure for deposition is between 10^{-6} and 10^{-7} torr, the tool is used by several different users and is opened often to change the target material. The chamber is baked out at 400˚C for 4 hours after every target change.

The most intense Si-O peak, in Figure 4.11, at around 1100 cm^{-1} is shifted to a higher frequency. It has been observed that a shift in this peak to a lower frequency is related to lower refractive index and/or lower density [32].

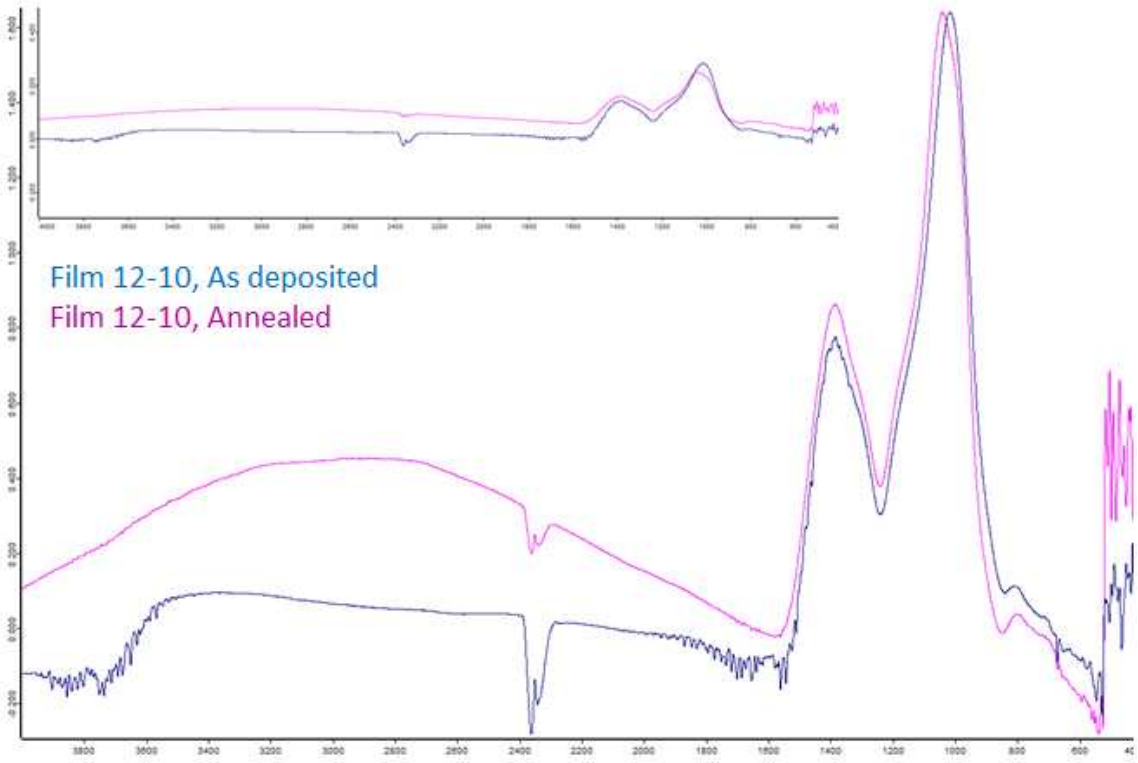

Figure 4.13: FTIR spectra taken in reflection mode of film 12/10 before and after annealing.

Film 12/10 was annealed for about 15 minutes at a temperature of 663˚C. The absorption spectra are shown in Figure 4.13. The inset figure is the originally scaled

spectra and the larger spectra have been magnified. The OH peak near 3600 cm^{-1} does not appear in the annealed spectrum. This is likely due to the evolution of molecular water from the film during annealing. The annealed Si-O peak shifts 25cm^{-1} to a higher frequency indicating an increase in film density which implies some relaxation of the oxide thin film structure. Otherwise, both spectra appear to be very close to one another.

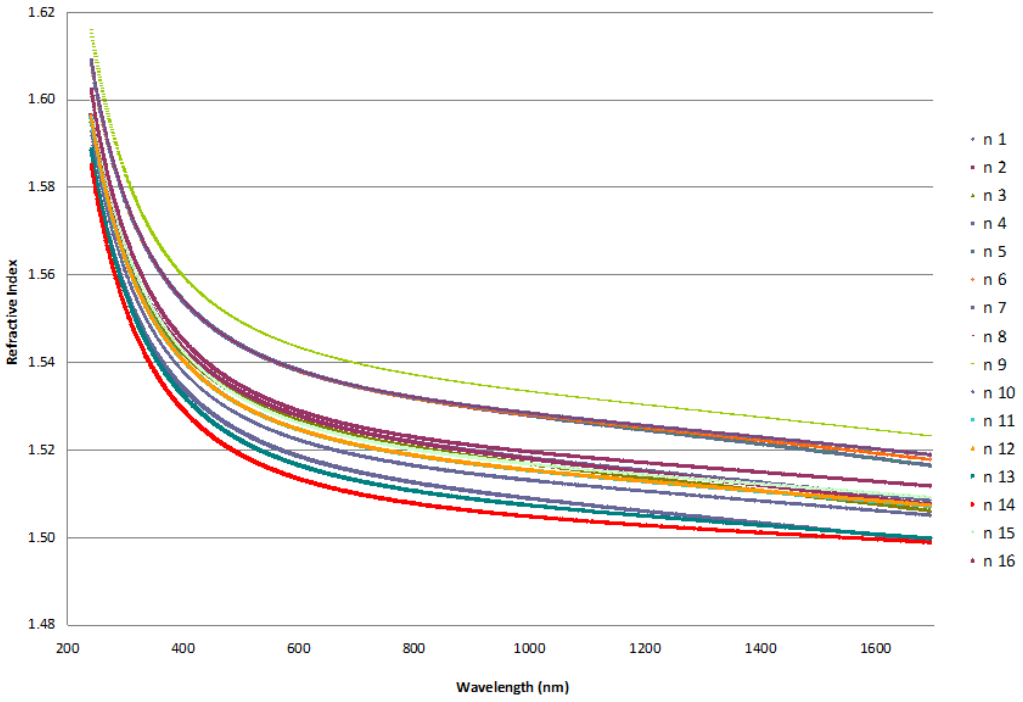

Figure 4.14: Dispersion curves measured using ellipsometry from film 11/05.

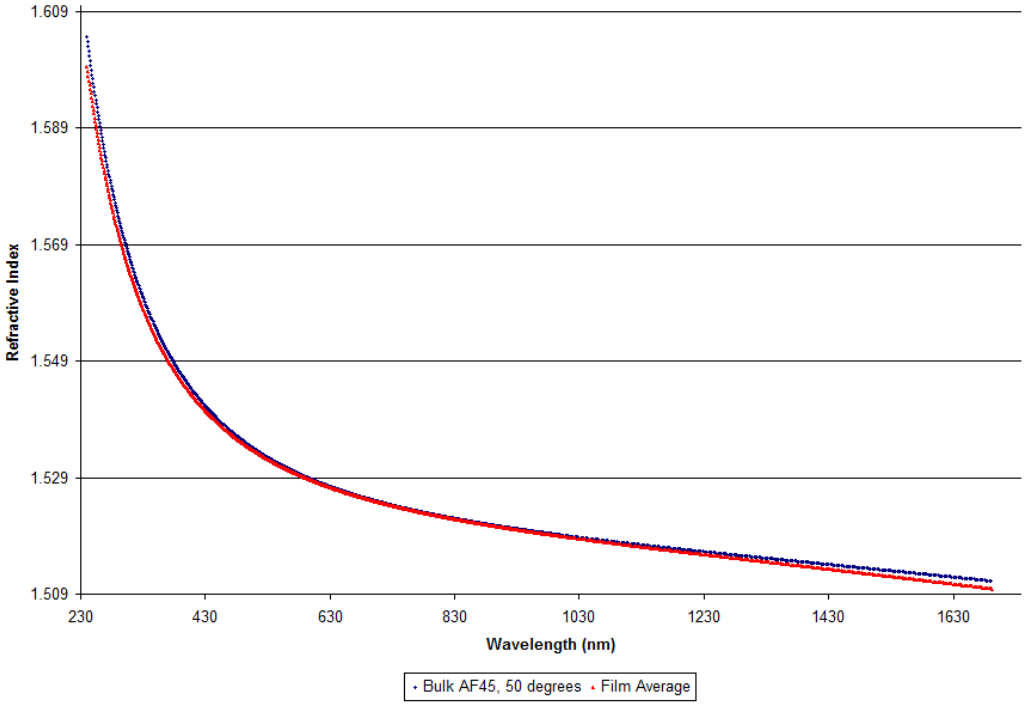

Figure 4.15: Dispersion curve of the average film, measured at 70 degrees, and bulk AF45, measured at 50 degrees.

Figure 4.14 presents the dispersion curves obtained at 16 different points on film 11/05 and provides additional information about the compositional and density non-uniformity across the wafer. Similarly, Figure 4.15 compares the average dispersion of the films, shown previously in Figure 3.6, to the dispersion measured with ellipsometry of bulk AF45. The bulk spectrum is slightly higher than that of the films.

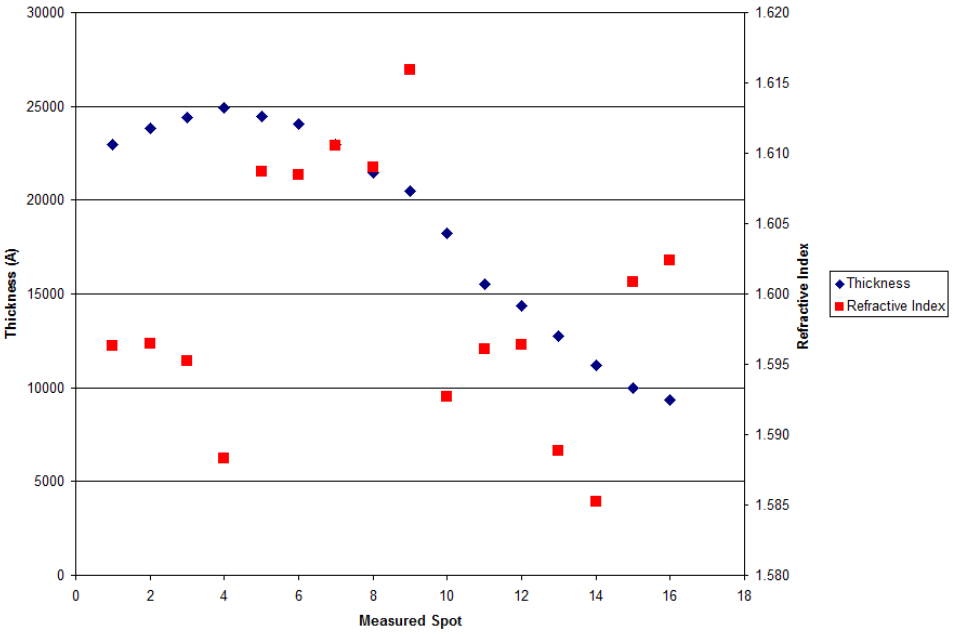

Figure 4.16: Thickness (Å) measured with ellipsometry compared to the respective refractive index calculated for each point at 240 nm.

Figure 4.16 shows that the refractive index trend does not directly correlate with composition or the predicted density trend. The barium content should be inversely proportional to thickness since the thickest area of the film is in the geometrical center of the processing chamber. The density of the film should be proportional to film thickness since the thickest parts of the film are subjected to the most ion bombardment. Composition and density would have contradictory effects with respect to refractive index. It is presumed that the complex interactions between non-uniform composition and density results in the varying refractive index with respect to position shown in Figure 4.16.

There is also the possibility of uncertainty in the measurement since only one angle was used and the section of film probed by the beam spot would not be completely uniform in thickness due to the thickness gradient.

4.2 DIELECTRIC BREAKDOWN DATA

All of the data taken in initial dielectric breakdown tests is displayed in Figure 4.17 as dielectric breakdown field versus thickness. The testing equipment has a lower detection limit around 600 V. The lower limit was determined by applying 250 V/s across the cathode and anode with no dielectric between them, essentially providing a short in the dielectric breakdown circuit. The resulting breakdown values were always less than or equal to 600 V. Most spots tested on film 12/08 broke down at or below the measurement limit of the tool. For this reason, film 12/08, the thinnest film deposited, is not shown on the plot due to skewing of the data.

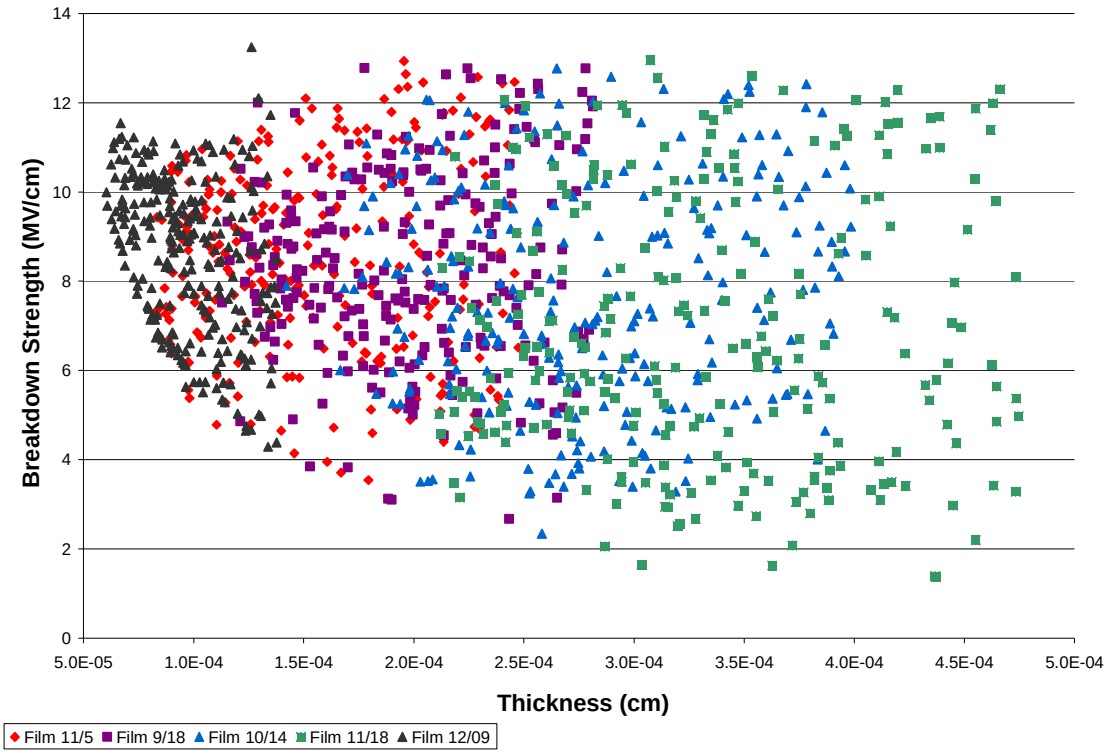

Figure 4.17: All useable data points, taken in the initial test, plotted as breakdown strength (MV/cm) versus thickness (cm). The plot does not include data with a breakdown voltage ≤ 604 V.

With respect to the remainder of the data, all breakdown spots failing at voltages less than or equal to 604 V were removed from plots and calculations. In Figure 4.17 there appears to be a well-defined lower field strength limit. This is an artifact of removing data points less than or equal to 604V and is not related to the sample properties.

During breakdown testing there were several observations made. Initial tests preformed on thinner samples, samples that broke down near the lower limit of the test, exhibited multiple discharges. There was an audible sizzle and many rapid discharges occurred. During the retests for these samples, there was often no visible or audible event occurring suggesting shorts. Despite the lack of detectable discharge some of these spots were measured to have a breakdown voltage greater than 604 V. Thicker samples exhibited a single discharge during breakdown for the majority of tested spots. The retest spots also behaved in a similar manner.

Table 4.4 lists the measured dielectric breakdown strengths and Weibull moduli as a function of each sample. Values for initial test and retest are displayed. As thickness decreases, the Weibull modulus and characteristic strength of each data set increases. The Weibull moduli of initial test samples are higher than in retest samples but there is no apparent trend between the characteristic strength of initial test values versus retest values. Figure 4.18 compares the Log [Characteristic strength (V/m)] versus the Log [Thickness (microns)] of the test and retest values. Both data sets show a reasonable agreement.

Table 4.4: Breakdown field values and corresponding Weibull moduli for data sets consisting of all test spots on a particular sample. Values for initial test and retest are displayed.

Film	Test or Retest	Weibull Modulus	Characteristic Strength (V/m)	Thickness Range (μm)	Average Thickness (μm)	Number of Data Points
12/09	Test	6.84	9.68 E8	0.6 – 1.4	0.99	217
11/05		4.84	9.51 E8	0.9 – 2.5	1.60	256
09/18		4.77	9.19 E8	0.9 – 2.8	1.97	237
10/14		3.52	8.58 E8	0.9 – 4.0	2.79	254
11/18		2.80	7.93 E8	2.0 – 4.8	3.32	252
12/09	Retest	5.97	9.57 E8	0.6 – 1.4	1.03	163
11/05		4.40	9.71 E8	0.9 – 2.5	1.62	233
10/14		4.09	8.89 E8	0.9 – 4.0	2.80	252
11/18		3.01	7.73 E8	2.0 – 4.8	3.33	247

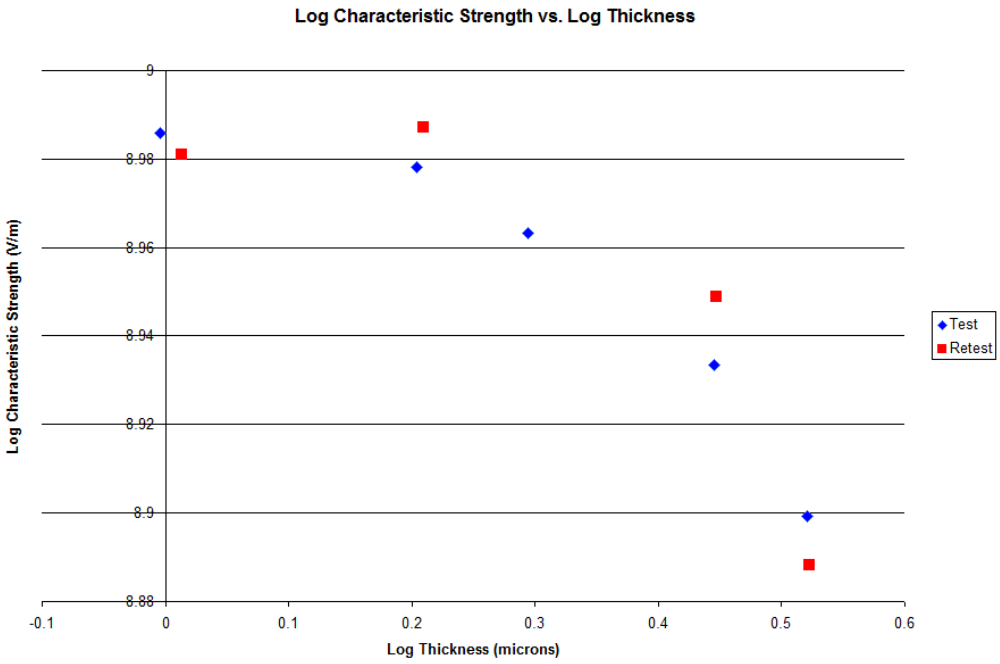

Figure 4.18: Log [Characteristic strength (V/m)] vs. Log [Thickness (microns)] of test and retest values. The thicknesses are averaged from all of the data within each film.

The agreement of characteristic strength for the initial and retest data (listed in Table 4.4 and displayed in Figure 4.18) is a good indication that graceful failure has taken place. When a breakdown event occurs, enough of the electrode area clears away to prevent a short when tested again. The agreement suggests a characteristic strength value intrinsic for this particular material. One would expect the breakdown strength to increase after the initial test since the first breakdown would affect the weakest spot between that set of electrodes. Since the second set of tests yield similar breakdown behavior then the measurements may either be in the intrinsic breakdown regime or may need to be tested several more times to see an appreciable increase in field strength.

All of the data points were compiled and divided into thickness ranges in order to calculate dielectric strength as a function of thickness. Table 4.5 lists the dielectric breakdown strengths and Weibull moduli as a function of thickness for the initial test values while Table 4.6 lists the same data for the retests. As with the data set divided up by sample, the Weibull modulus and characteristic strength of each data set increases with decreasing thickness. Figure 4.19 compares the highest and lowest Weibull distributions of the data sets. Figure 4.20 compares the Log [Characteristic strength (V/m)] versus Log [Thickness (microns)] of the test and retest values listed in Tables 4.5 and 4.6.

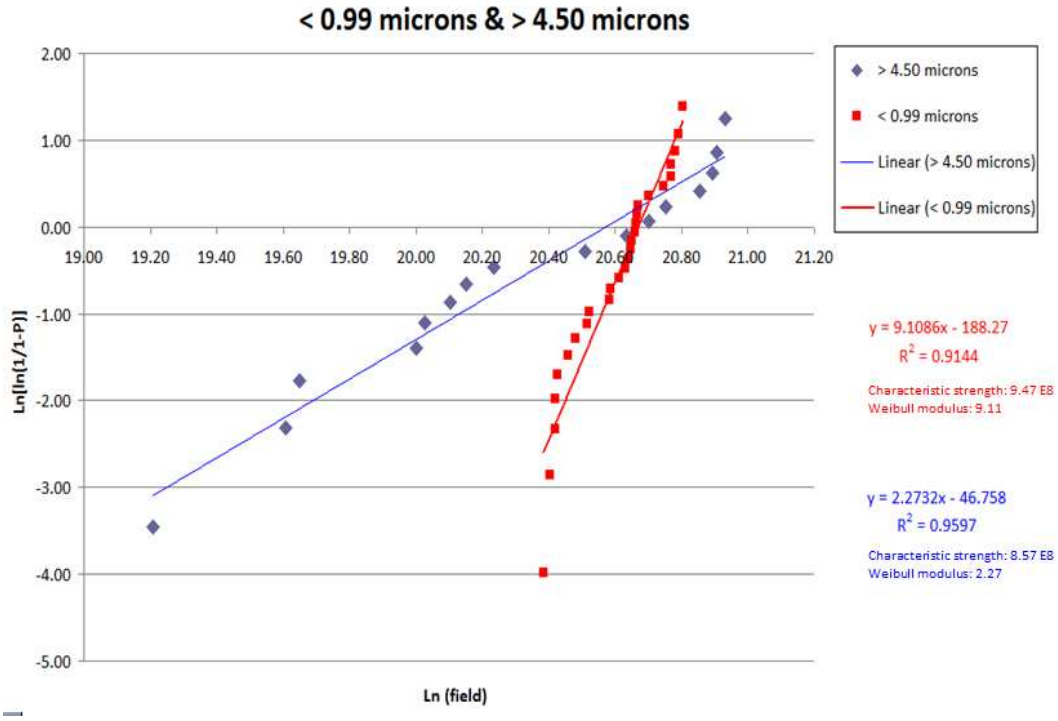

Figure 4.19: Weibull moduli for two data sets, breakdown spots below 0.99 microns and above 4.50 microns. These data sets were chosen to compare a high Weibull modulus distribution and a low Weibull modulus distribution.

Table 4.5: Breakdown field values and corresponding Weibull moduli for data sets consisting of all test spots within a particular thickness range. Values for initial test are displayed.

Thickness Range (μm)	Average Thickness (μm)	Weibull Modulus	Characteristic Strength (V/m)	Number of Data Points
< 0.99	0.92	9.11	9.47 E8	27
1.00 – 1.49	1.28	6.86	9.15 E8	139
1.50 – 1.99	1.78	4.60	9.25 E8	180
2.00 – 2.49	2.25	3.82	8.95 E8	240
2.50 – 2.99	2.72	3.18	8.32 E8	161
3.00 – 3.49	3.23	2.84	8.27 E8	111
3.50 – 3.99	3.73	2.87	8.32 E8	91
4.00 – 4.49	4.25	2.52	8.65 E8	35
> 4.50	4.64	2.27	8.57 E8	16

Table 4.6: Breakdown field values and corresponding Weibull moduli for data sets consisting of all test spots within a particular thickness range. Values for retests are displayed.

Thickness Range (μm)	Average Thickness (μm)	Weibull Modulus	Characteristic Strength (V/m)	Number of Data Points
< 0.99	0.94	9.82	9.45 E8	21
1.00 – 1.49	1.24	5.67	9.39 E8	80
1.50 – 1.99	1.78	4.18	9.95 E8	93
2.00 – 2.49	2.26	3.63	9.14 E8	153
2.50 – 2.99	2.74	3.75	7.99 E8	127
3.00 – 3.49	3.23	3.25	8.25 E8	111
3.50 – 3.99	3.74	3.18	8.81 E8	90
4.00 – 4.49	4.24	2.53	7.94 E 8	35
> 4.50	4.64	2.27	6.81 E8	16

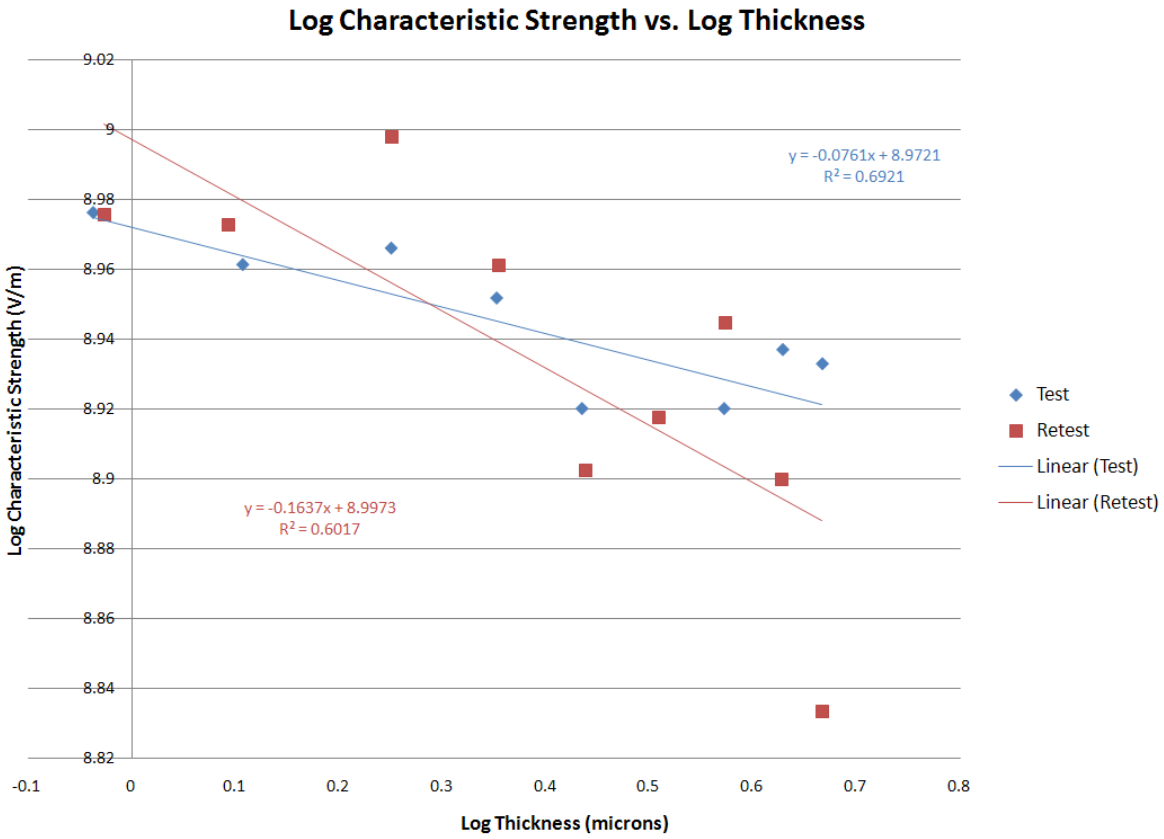

Figure 4.20: Log [Characteristic strength (V/m)] vs. Log [Thickness (microns)] of test and retest values. The thicknesses are averaged from all of the data within each thickness interval.

There is a bigger difference between the test and retest data when plotted based on thickness as opposed to sample. This behavior may be related to the large spread observed in Figure 4.17. Since both figures mix spots from different samples in each data set, the differences in composition and density may be affecting the modulus and agreement.

It is also noted that the average thickness of the retest values is slightly higher than that of the initial test values. The increase in average thickness for retest spots may suggest that most of the spots acting as shorts (and therefore removed from the data set) were thin. Removing data points has the potential of skewing the data in one direction or the other. It is a reasonable assumption that removing data points where breakdown occurs less than or equal to 604 V does not have a significant effect. If a thin and a thick spot both have a breakdown voltage of 500 V, removing the thin spot will be removing a high field spot while removing the thicker spot from the data will be removing a low field spot. Low voltage breakdown spots correspond to thicknesses throughout the range of thicknesses and are not confined to either end of the field range. This might explain the slight trend noticeable at the high field end of the data displayed in Figure 4.17. The thinner the sample, the more data was removed and therefore the more a ‘trend’ stands out.

Figures 4.21-4.25 show what happens to the film on a microscopic level after breakdown occurs. Figure 4.21 is a cross section of a film taken after breakdown. Each pair of optical/FE-SEM figures represents films with similar thickness but dissimilar breakdown voltage. The first two spots were taken from film 11/05 (V_b ~ 1139 V, 543 V) and the last two spots were taken from film 11/18 (V_b ~ 3905 V, 497 V).

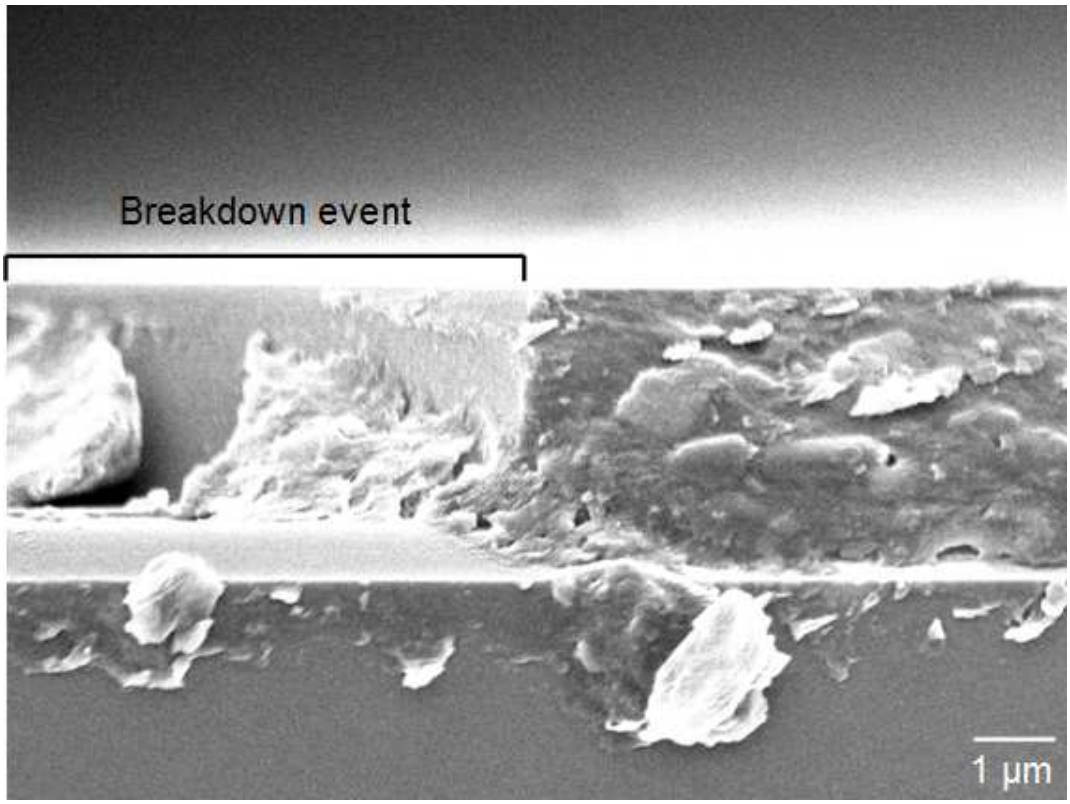

Figure 4.21: FE-SEM cross section of a breakdown event.

Figure 4.21 shows a cross section of a film after breakdown testing. There is a large amount of debris present on the film. It appears that there is a volume of the film no longer present due to breakdown. It is unclear as to whether the glass has been removed all the way to the glass-platinum interface or if some remains. In the next 4 Figures, it appears that some part of the film stack has been melted during the course of breakdown. It may be possible that there is some glass remaining at the interface that had been melted during breakdown but cannot be confirmed just by referring to Figure 4.21.

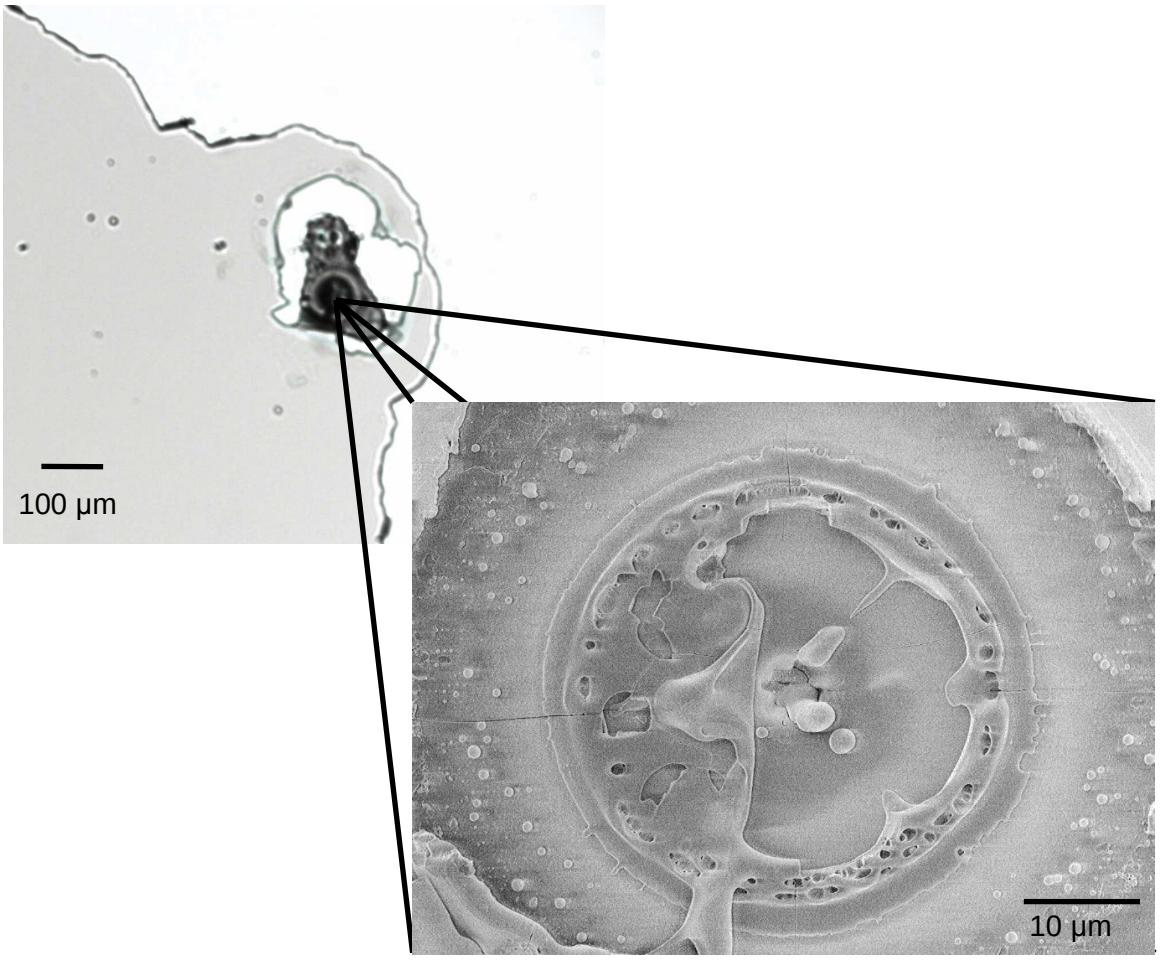

Figure 4.22: FE-SEM and optical microscope image of a breakdown event on a sample 1.04 microns thick that broke down at 1139 V.

There is a 1.8 mm diameter spot of cleared top electrode material in the center of the electrode after breakdown of the sample in Figure 4.22. There are two breakdown events one on the edge of the cleared area and one in the surrounding platinum (not shown in the optical image). In the FE-SEM image, it appears that the glass or platinum electrode has melted, bubbled and cracked.

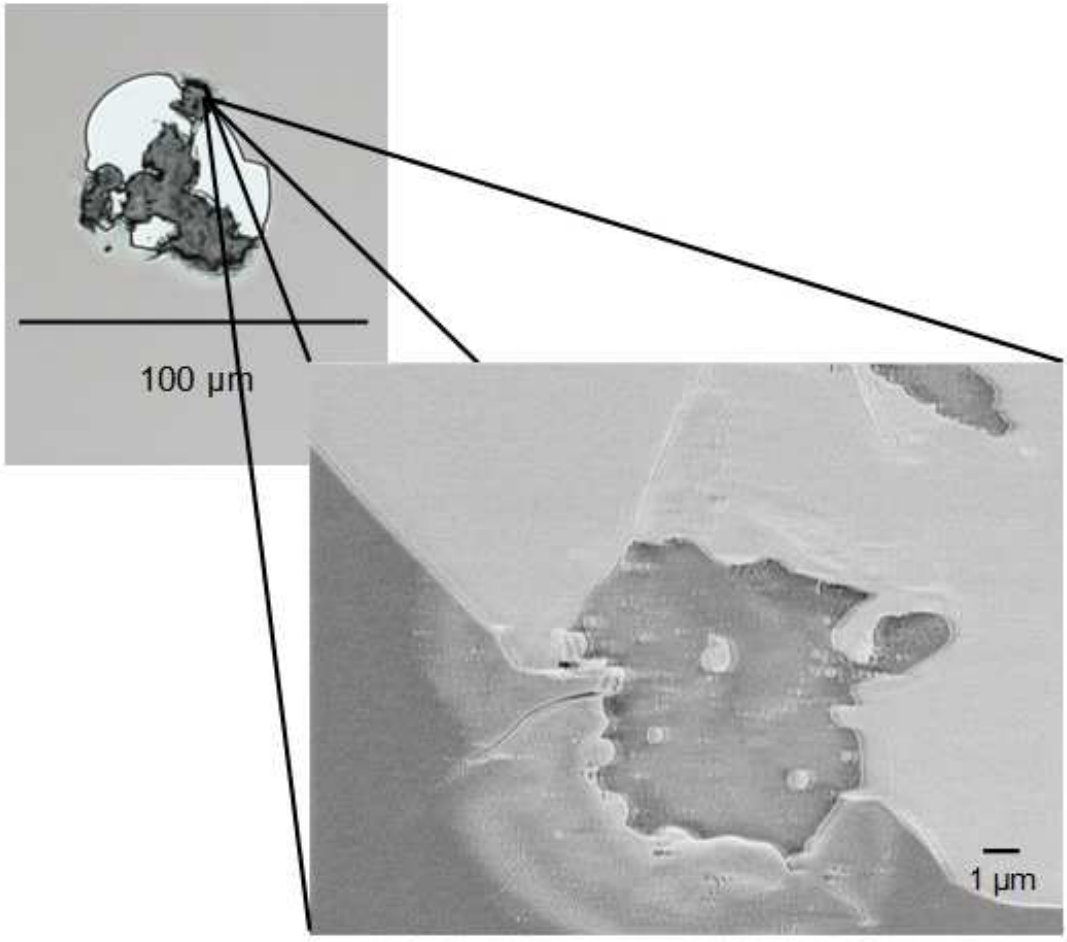

Figure 4.23: FE-SEM and optical microscope image of a breakdown event on a sample 0.98 microns thick that broke down at ≤ 543 V.

After breakdown of the sample in Figure 4.23, there were several small pinholes in addition to the spot shown on the optical microscope image. Most of the platinum electrode was cleared away. In the FE-SEM images it appears that the top platinum electrode remaining near the spot (lighter portion) has melted back and there is slight melting of the glass or bottom platinum electrode (darker portion) indicated by the deformation.

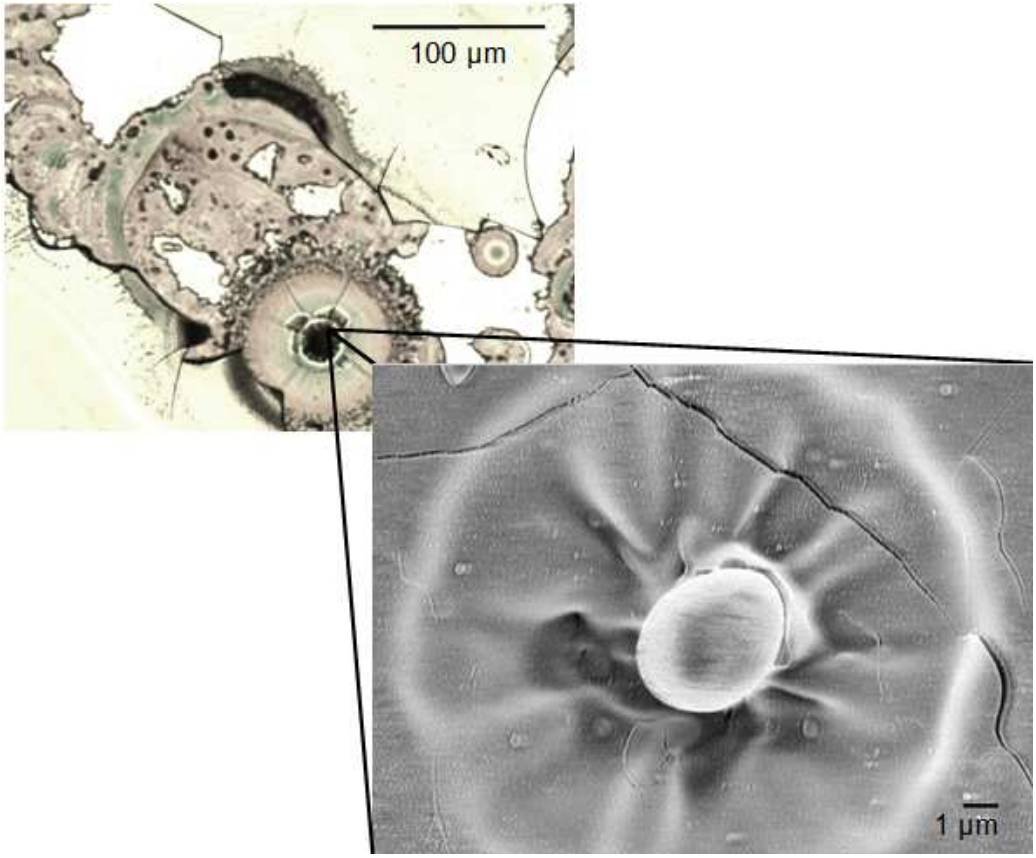

Figure 4.24: FE-SEM and optical microscope image of a breakdown event on a sample 3.07 microns thick that broke down at 3905 V.

Figure 4.24 shows what appears to be the melting of glass or platinum (FE-SEM image) within a well-defined breakdown spot (optical image). The breakdown event exhibits a large cleared top electrode area like in Figure 4.22 but also shows an overlapping area of hazy, crescent shaped features. It is difficult to know if these features are comprised of glass, platinum or a combination of the materials. Within the hazy area there are some breakdown events, only one of which is observable in the figure. There is also a cluster of small breakdown events within the cleared area (not shown).

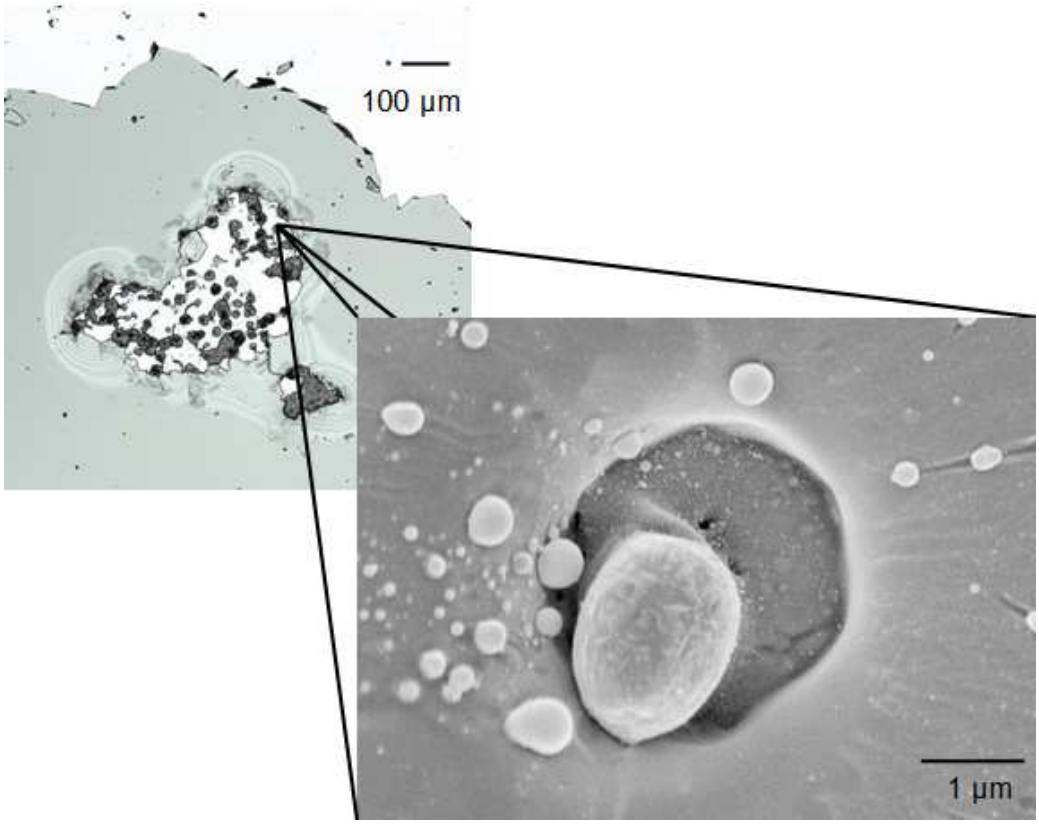

Figure 4.25: FE-SEM and optical microscope image of a breakdown event on a sample 3.03 microns thick that broke down ≤ 497 V.

In Figure 4.25 there is one example of a small breakdown cluster (optical image) within the cleared electrode area about the same diameter as in Figure 4.22. There are several other breakdown clusters on this particular electrode. The FE-SEM image again indicates melting of the glass or bottom platinum electrode. Additional images taken of the previous spots can be found in the Appendix.

Breakdown events were not consistently found in any one particular location on the electrode spot. Breakdown events occurred with a variety of shapes and configurations, some of which are shown in the above figures. One characteristic to note

is that breakdown rarely occurred directly under the probe. This is a good indication that breakdown did not occur due to mechanical stress imposed on the sample by the probe.

Based on Figures 4.21-4.25 and the observations of discharge during the test, it seems that low breakdown voltage spots lead to several separate breakdown events while higher voltage spots are more likely to clear out a large section of electrode with 1 or 2 breakdown events present. This phenomenon is not strictly a characteristic of thin film capacitors. It was observed in the Lee study that electrode clearing can be related to the breakdown field of the material in addition to other variables [13].

Dielectric breakdown of bulk AF45 was measured by other investigators [13, 14] and summarized below. In each case the glass was thinned down using diluted HF acid. Slight variations were present such as the use of ultrasonication during etching in the Lee study but not in the Smith study. Table 4.7 lists the characteristic strengths, Weibull moduli and thicknesses of glass samples from Lee's study and table 4.8 lists information measured by Smith.

Table 4.7: Weibull moduli and characteristic strength values of bulk glass taken from the Lee paper. [13]

Thickness (μm)	Weibull Modulus	Characteristic Strength (V/m)	Number of Data Points
6	7.81	1.16 E9	8
10	9.01	1.08 E9	35
15	9.41	1.05 E9	36
20	7.30	1.03 E9	38
25	6.66	8.31 E8	37
30	7.80	7.58 E8	34
50 (AR)	8.86	4.17 E8	36

Table 4.8: Weibull moduli and characteristic strength values of bulk glass taken from the Smith paper. [14]

Thickness (μm)	Weibull Modulus	Characteristic Strength (V/m)	Number of Data Points
4.8	11.61	1.28 E9	25
11.3	6.70	1.10 E9	24
12.3	9.42	1.10 E9	20
13.1	9.30	1.20 E9	23
18.6	10.70	1.20 E9	23
23	5.79	8.49 E8	15
35.2	5.32	6.19 E8	16
47 (AR)	4.80	5.20 E8	16

The thickness measurements were also conducted differently. In the Lee study thickness was measured using a very sensitive micrometer while Smith used FTIR spectroscopy to measure interference fringes and calculate the thickness. The Weibull moduli and characteristic strength measured in the Lee study tend to increase as thickness decreases. There are some values that are out of placed based on the theory of decreasing thickness yielding increasing characteristic strength. The same trends are observed in the Smith study. The Log [Characteristic strength (V/m)] versus Log [Thickness (microns)] of AF45 from all studies is plotted in Figure 4.26 to allow for a clear comparison of the data. Data from the Lee and Smith study are consistent with one another. The thin film values are lower by about 20%.

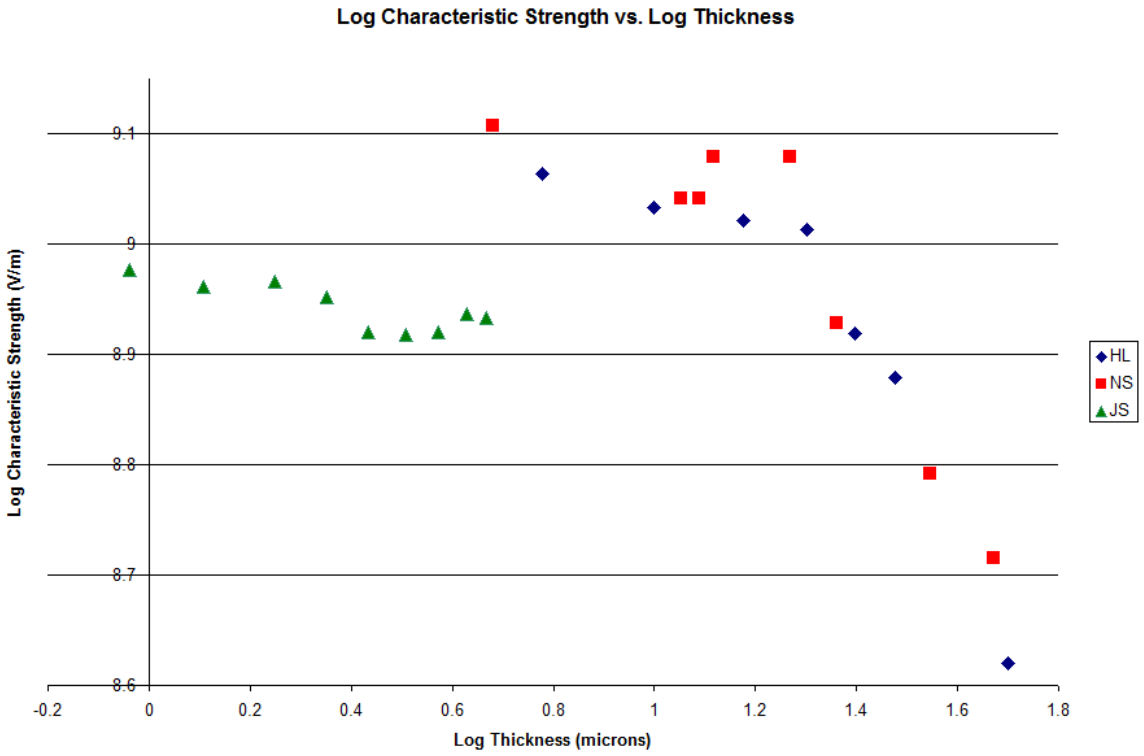

Figure 4.26: Log [Characteristic strength (V/m)] vs. Log [Thickness (microns)] of bulk glass characteristic strength taken from Table 4.6 and 4.7 and thin film test values from Table 4.4. The thin film thicknesses are averaged from all of the data within each thickness interval. [13, 14]

4.3 DIELECTRIC BREAKDOWN COMPARISON

The Lee and Smith studies measured remarkably high breakdown strengths for bulk AF45. Despite slight differences in sample preparation and thickness measurements, both data sets have reasonable agreement of dielectric breakdown strength as a function of thickness. According to the thickness dependence of breakdown, AF45 thinner than 5 microns should have increased breakdown strength as thickness decreases or the value should level off indicating the intrinsic breakdown strength. The maximum breakdown

strength measured for the AF45 thin films was about 9.5 MV/cm for a 1 micron thick film.

It can be suggested from looking at Figure 4.26, that the bulk glass data indicates two regions. At around Log [Thickness (microns)] of 1.3 the data appears to have changed slope from a steep slope closer to -1 to a shallow slope around -0.1. This could indicate a change from thermal breakdown to avalanche breakdown. The glass would be sufficiently thin around this transition point that heat buildup would not limit the breakdown strength. If this is the case, the glass should have a dielectric breakdown strength between 12-15 MV/cm at a thickness of 1 micron. This estimated breakdown range was determined by extrapolation of the data; the best fit trend line calculated from data points less than Log [Thickness (microns)] of 1.3 was used.

There are several potential reasons why the dielectric breakdown strength of the thin films is not in the predicted 12-15 MV/cm range. Some are a related to the measurements while others are due to the material.

The method by which thickness was measured can lead to error in the breakdown data. Since it was observed that refractive index varied depending on where on the sample it was measured, there is a certain amount of error associated with the average dispersion used to calculate the film thickness. Chapter 3 described how an average dispersion was calculated from the dispersion measured at sixteen different spots across film 11/05. The average dispersion was used by the reflectometer to generate a thickness map of each film.

The highest and lowest dispersion curves were used in the same manner to calculate the error propagated to the thickness measurements associated with using an

average dispersion curve. A 1-2% difference in thickness from the average value was measured. This influenced the calculated breakdown strength by a maximum of 0.21 MV/cm based on the variability in thickness. Using an average dispersion to calculate thickness therefore did not have a significant effect on the breakdown strength of the films.

The testing conditions were also problematic. Aside from the reduced sensitivity for thin dielectrics exhibited by the breakdown equipment, the fluid was contaminated. Table 4.2 lists the impurities present on the film analyzed after submersion in the dielectric breakdown fluid. Any influence testing conditions may have had on breakdown strength would manifest in both the film and the bulk glass data.

As was already mentioned, a peak due to water vibrations was present in the film spectrum as well as a shift in the Si-O peak compared to the bulk glass. Water in or on the film would reduce the breakdown strength by acting as a charge carrier through the glass. The lower film density would increase the mobility of these charge carriers to facilitate conduction.

Due to the nature of thin film deposition, the atoms or clusters of atoms being removed from the target may not have energy to diffuse into the most energetically favorable position. The resulting film will have a higher fictive temperature structure, increasing the probability of having defects such as voids, stresses, strained bonds, or local areas of compositional or network structural non-uniformities. The presence of nano and microscopic voids and other structural defects in, or on the surface of, the films, has traditionally reduced breakdown strength in many dielectrics. Inclusions in the films, as well as surface roughness can act to concentrate the field at that site.

Referring back to Figures 4.2 and 4.3 the surface of the film does not appear to be as smooth as the glass tested by Lee and Smith but did have a roughness on the order of the etched glass. Any affect this degree of surface roughness would have on the films in reducing dielectric breakdown would be present for the films and the bulk glass. There were also features on the surface approximately 20 nm in diameter. Significantly sized surface features can act to shadow portions of the surface during electrode deposition resulting in trapped voids or an uneven electrode. The films were also synthesized and tested in air. After glass film deposition, the films were measured with ellipsometry and reflectometry before electrode deposition. It was therefore not possible to keep the film surface completely clean and free of dust. Dust could have been trapped between the film and the electrode.

It was observed that the composition varied as a function of position. It was also speculated that there was a change in film density as a function of position. Such regions could focus or magnify the applied field. The inhomogeneity of the films may also contribute to a decrease in dielectric breakdown strength by enhancing structural defects. The variation of composition and structure associated with each film and between the films may have lead to the low Weibull modulus values.

CHAPTER 5

SUMMARY AND LESSONS LEARNED

Glass thin films fabricated with RF magnetron sputtering do not resemble their target glass based on compositional and structural measurements. They appear to be microstructure free but do vary in composition across the substrate. Density differences are present between the film and the bulk due to deposition. Techniques sensitive to bonding such as nuclear magnetic resonance would be useful in determining how the network of this set of glass films is bonded on an atomic scale and if the bonding is significantly different from that of the bulk glass. Transmission electron microscopy may be sensitive enough to observe smaller voids or columns than cannot be observed in FE-SEM.

The maximum dielectric breakdown strength measured for glass thin films was 9.5-10 MV/cm compared to 12-13 MV/cm for the bulk glass. The presence of water and the reduced density the film may have lead to the reduction in breakdown strength. Compositional and density non-uniformity may have also contributed to a reduction in dielectric breakdown strength in addition to reducing the Weibull moduli values. The surface roughness measured as well as potential debris trapped on the surface and the presence of nano and microscopic voids and structural defects could have contributed significantly to reduction of breakdown strength.

Overall these films were not ideal samples to deduce intrinsic dielectric breakdown strength of bulk AF45. The lack of compositional uniformity made interpretation and reproducibility of the dielectric measurements difficult. There are several steps that would need to be taken in order to improve the quality of the thin films. Using sample rotation, a smaller substrate, a shorted target-to-substrate distance and post deposition annealing would all help to improve compositional and structural uniformity in addition to creating a more dense film. Although the thickness gradient allowed for a variety of thicknesses to test, it made measuring thickness difficult and introduced a level of uncertainty into the measurements. Using a uniform well defined thickness would make clean room fabrication of the complete sample more feasible by eliminating the need to measure thickness before electrode deposition. This would prevent surface contaminates or hydration from being trapped under the electrode. A system that allowed for ion beam deposition could aid in more uniform films by removing the film from the plasma. Since barium was the most depleted of the elements in the films, using a supplemental BaO target during deposition could help maintain better compositional uniformity while still allowing the use of a commercial glass target.

In order to obtain a better understanding of the dielectric breakdown behavior of glass thin films, a more sensitive testing device should be used. The larger DC source was used to maintain consistency in the testing procedure with the previous tests on AF45 glass. Since bulk glass is significantly thicker, a larger voltage is needed to reach breakdown. Films less than a micron in thickness are more reliably tested on a less powerful, more sensitive source.

It would be interesting to deposit another alkali-free glass as a film to see how sensitive the dielectric breakdown properties are to network composition and polarizability of the alkali earth modifiers. Nippon Electric Glass OA10G has also been observed to have high dielectric breakdown strength. The glass is also an alkali-free boroaluminosilicate but has four more divalent cation modifiers, in addition to barium, than Schott AF45.

APPENDIX A

ADDITIONAL THICKNESS MAPS

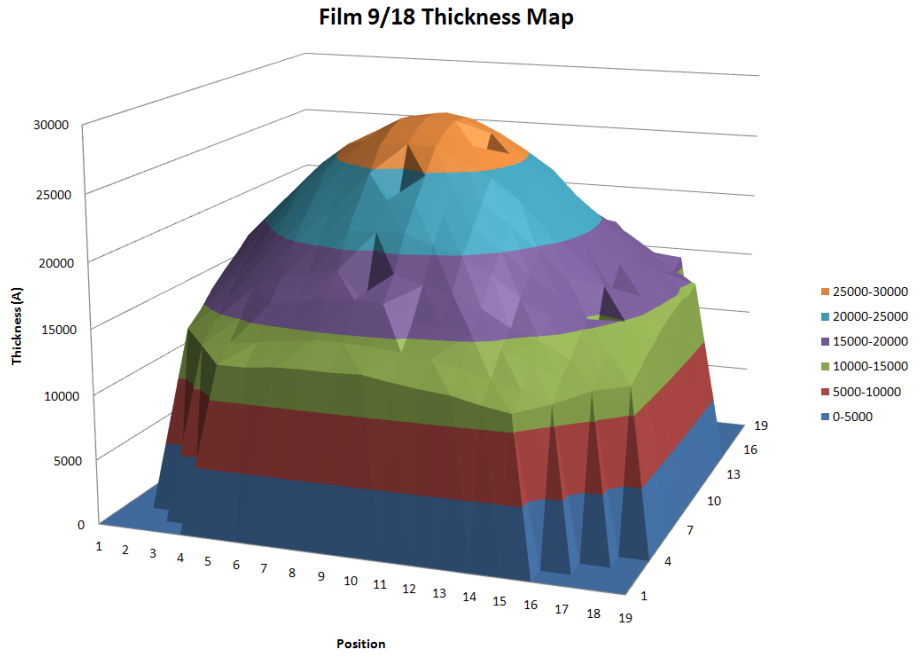

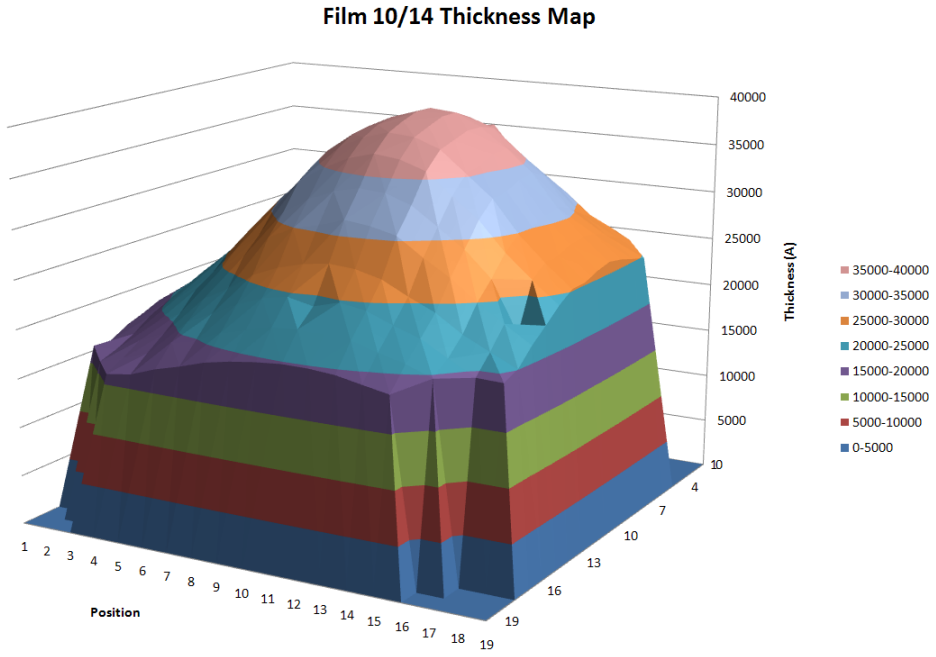

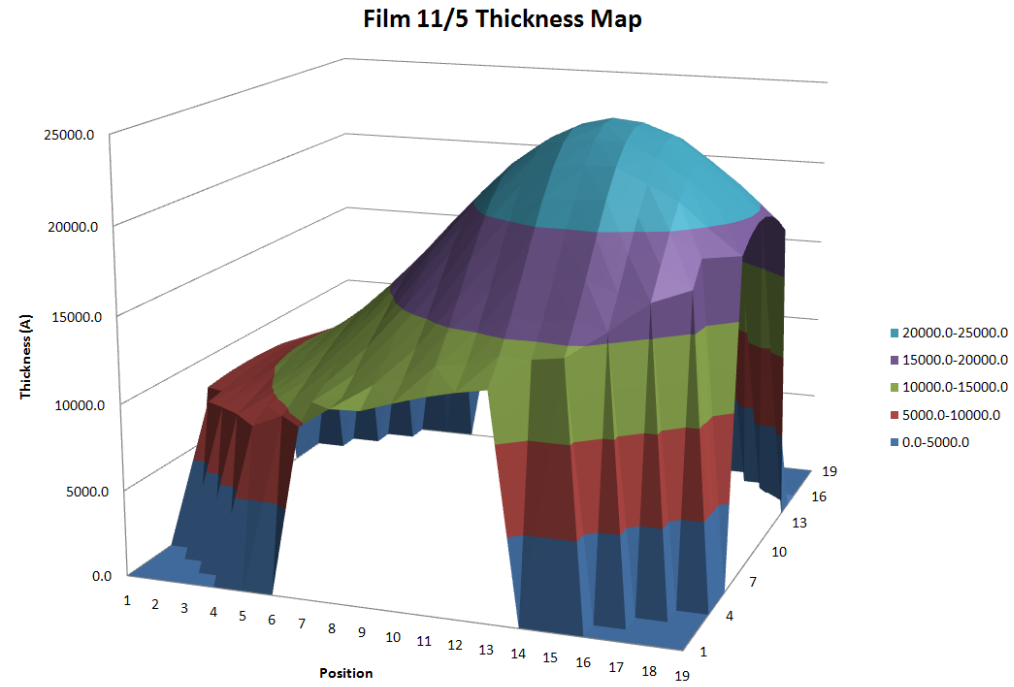
Film 11/5 Thickness Map
Thickness (A)
25000.0
20000.0
15000.0
10000.0
5000.0
0.0
1 2 3 4 5 6 7 8 9 10 11 12 13 14 15 16 17 18 19
Position
1 4 7 10 13 16 19
20000.0-25000.0
15000.0-20000.0
10000.0-15000.0
5000.0-10000.0
0.0-5000.0

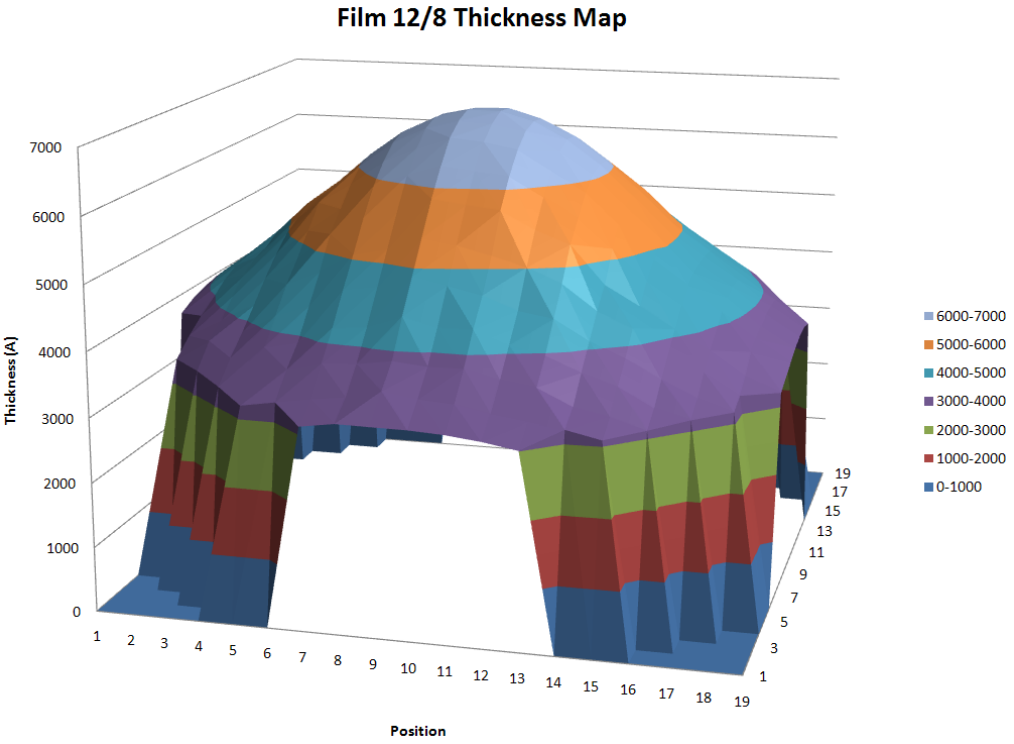
Film 12/8 Thickness Map
Thickness (A)
7000
6000
5000
4000
3000
2000
1000
0
1 2 3 4 5 6 7 8 9 10 11 12 13 14 15 16 17 18 19
Position
1 3 5 7 9 11 13 15 17 19
6000-7000
5000-6000
4000-5000
3000-4000
2000-3000
1000-2000
0-1000

Film 12/10 Thickness Map

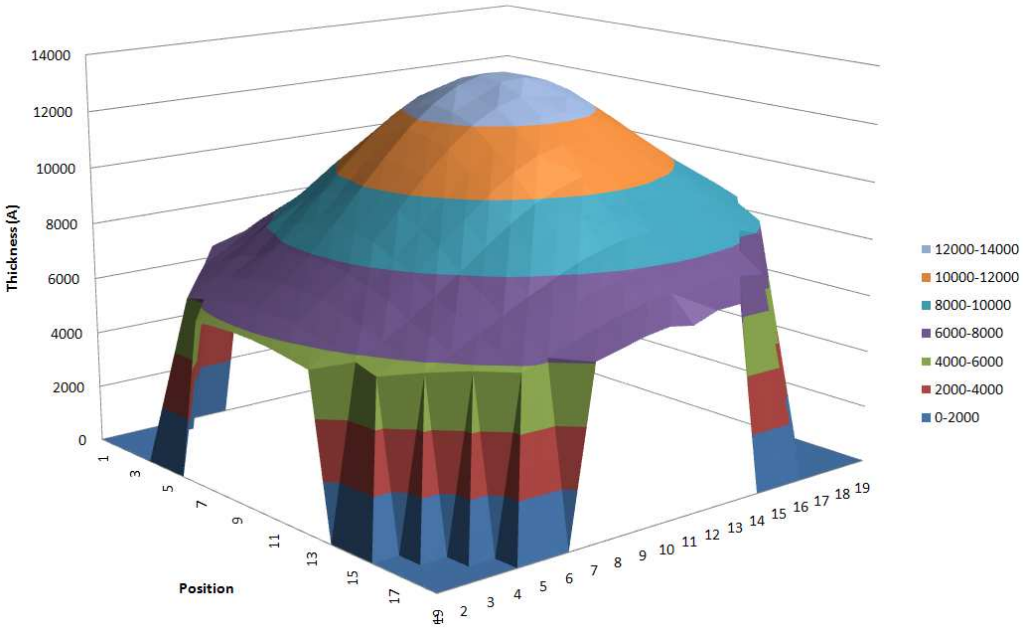

Film L1 Thickness Map

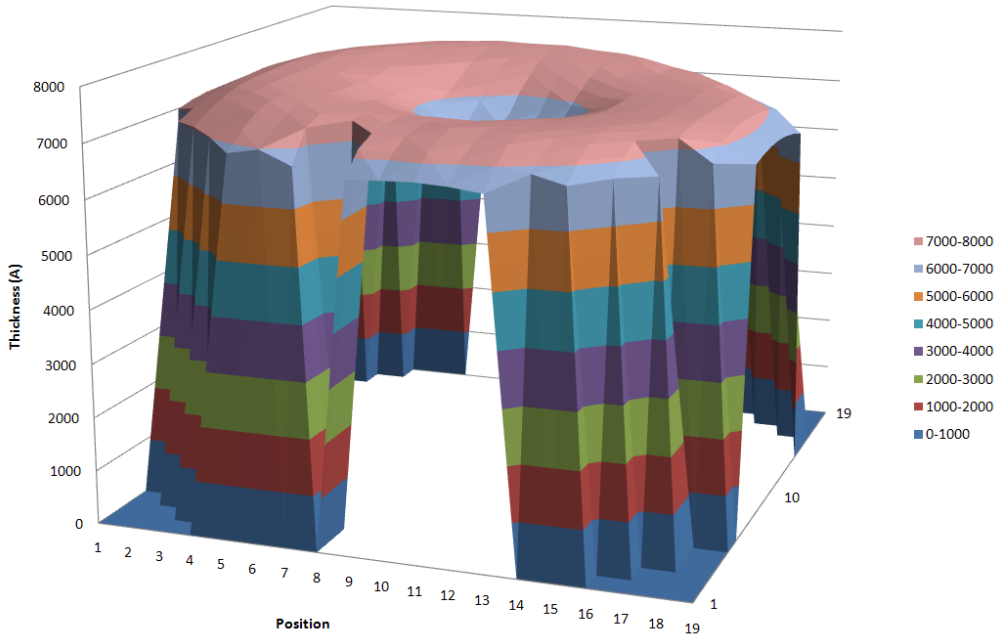

APPENDIX B

COMPOSTIONAL DATA

The compositional data in this table was taken from films measured after being submerged in the dielectric breakdown fluid. The amount of impurities on the surface increases the difficultly obtaining accurate compositional data. The trends observed in Table 4.1 are present in the compositional data of the following table.

Film	Characterization Method	Mol %					Atomic %	Additional Impurities
		SiO_2	B_2O_3	BaO	Al_2O_3	As_2O_3	C	
12/08E	High res XPS	72.0	12.6	5.0	10.2	0.2	5.6	Mg, Na, Cu, F, Ca, K, Pt
11/18C	High res XPS	72.5	15.3	2.9	9.0	0.2	4.7	Mg, Na, Cu, F, Ca, K, Pt
11/18E	High res XPS	71.9	12.5	5.6	9.8	0.2	5.1	Mg, Na, Cu, F, Ca, K, Pt
9/18E	High res XPS	71.4	8.0	7.9	12.3	0.4	22.9	Mg, Na, Cu, F, Ca, K, Pt
9/18C	High res XPS	74.2	10.78	4.9	9.9	0.3	9.7	Mg, Na, Cu, F, Ca, K, Pt
11/18C	EPMA	60.8	20.8	7.0	11.2	0.2	n/a	Ar
L2C	High res XPS	76.7	10.9	3.8	8.6	0	5.2	Ar, F, N
L2E	High res XPS	80.8	6.3	5.2	7.7	0	5.4	Ar

APPENDIX C

DIELECTRIC BREAKDOWN EVENTS

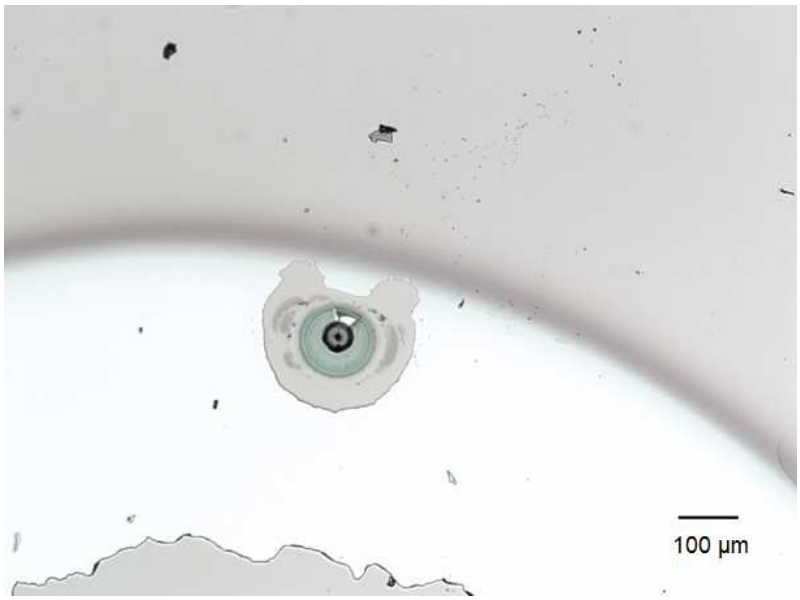

Optical image showing dielectric breakdown event not included in Fig 4.22

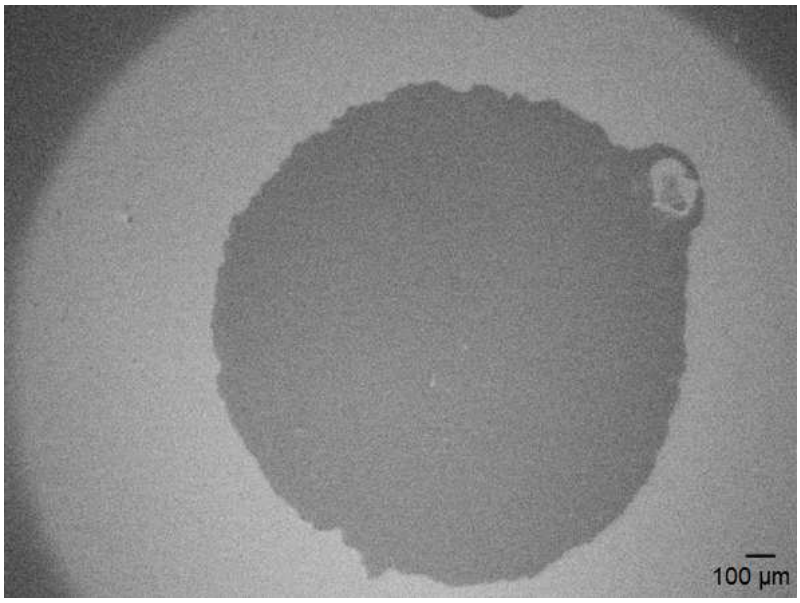

Lower magnification FE-SEM image of Fig 4.22

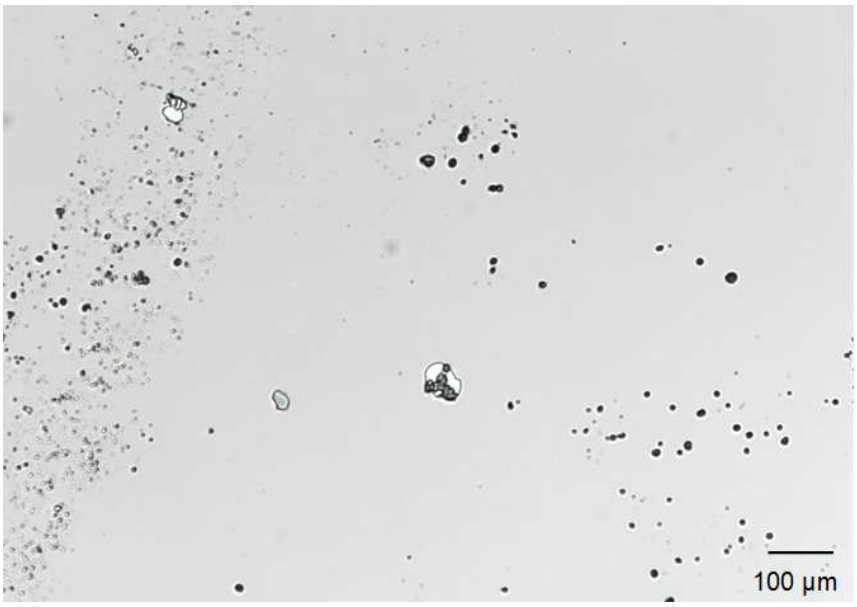

Lower magnification of optical image shown in Fig 4.23

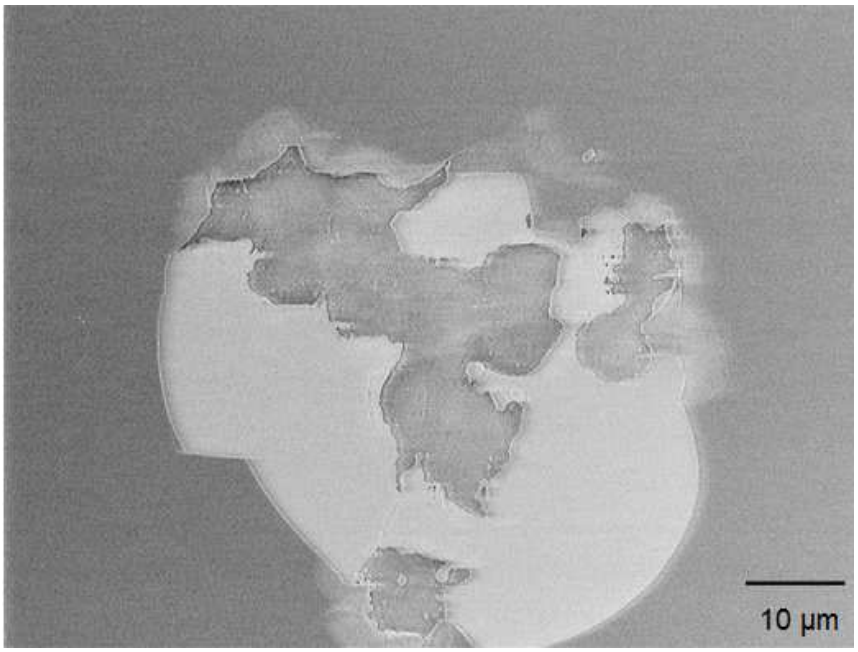

Lower magnification FE-SEM image of dielectric breakdown event shown in Fig 4.23

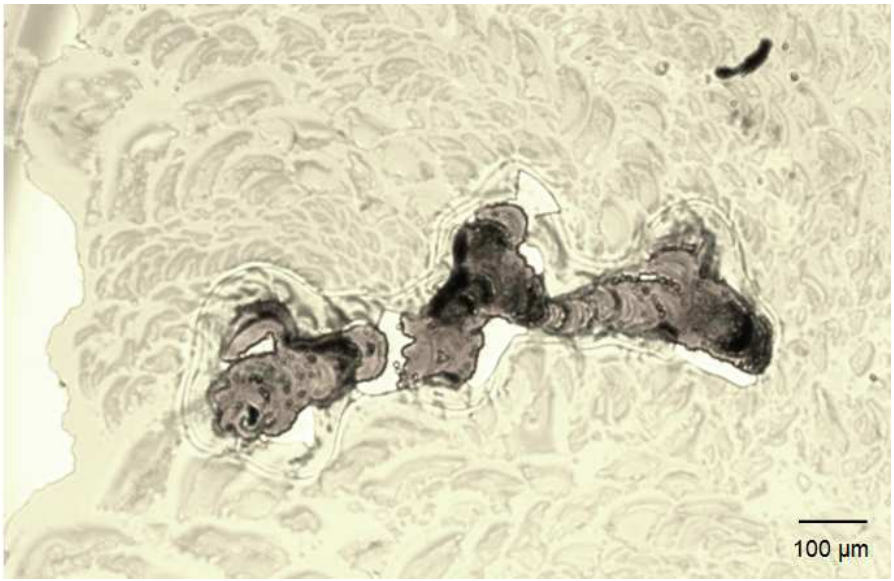

Optical image of ‘hazy region’ not shown in Fig 4.24

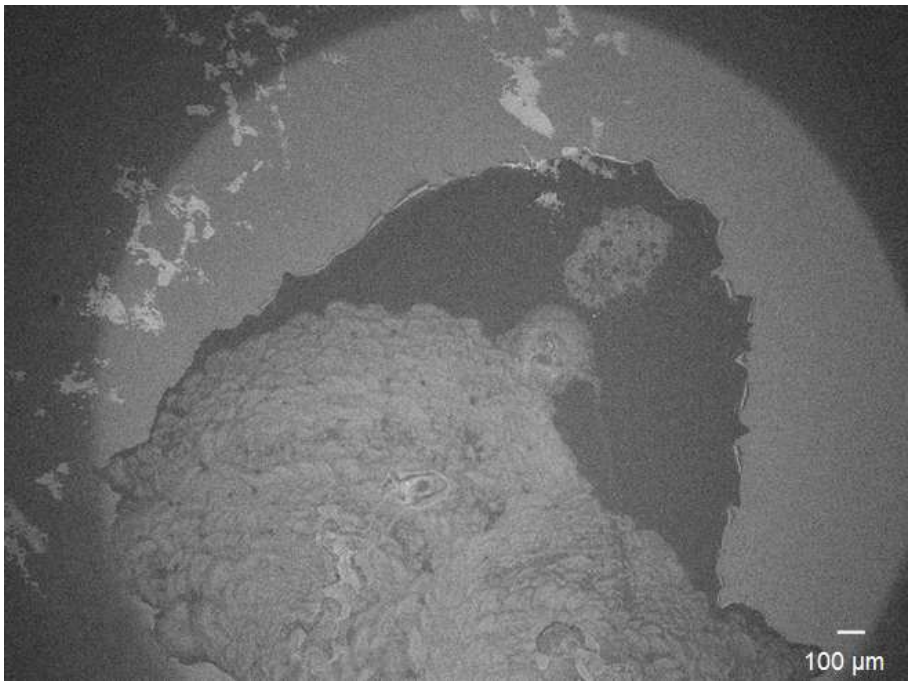

Lower magnification FE-SEM image of dielectric breakdown spot shown in Fig 4.24

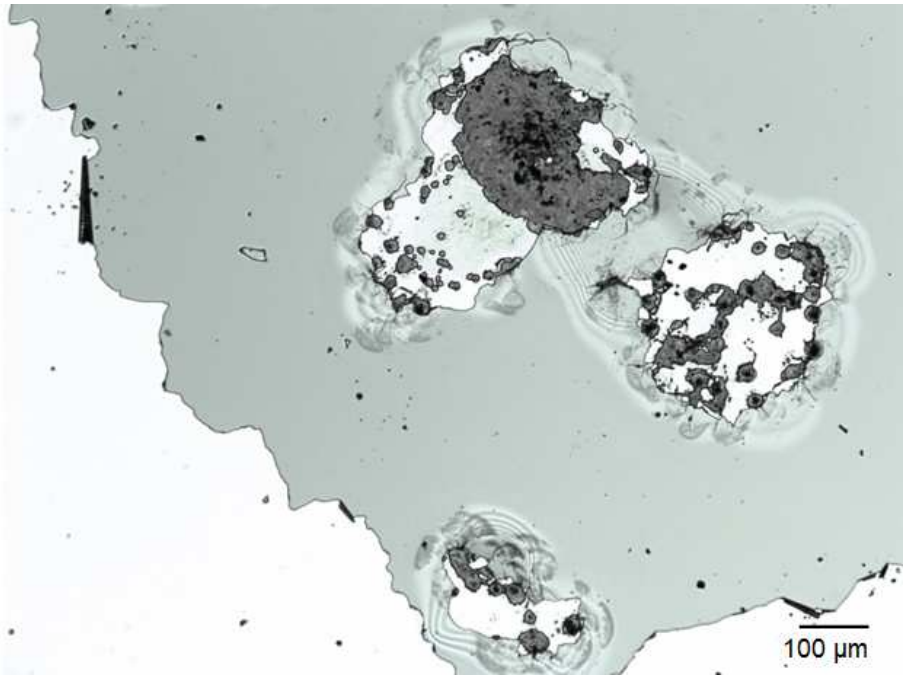

Optical image of additional dielectric breakdown event clusters within the cleared electrode, not shown in Fig 4.25

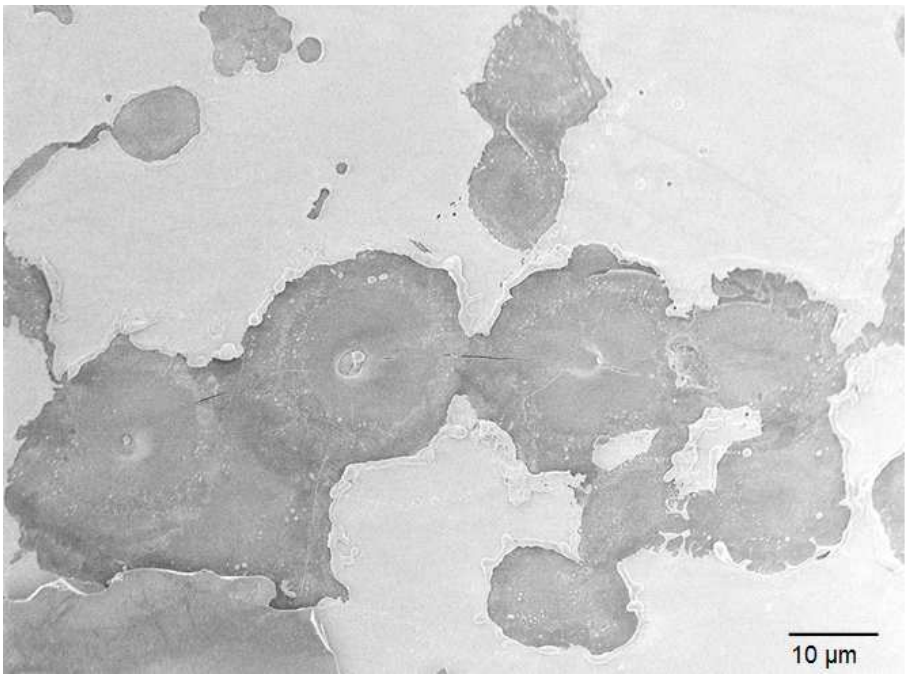

FE-SEM image of dielectric breakdown event clusters corresponding to Fig 4.25

BIBLIOGRAPHY

1. Huebner, W., et al., *High Breakdown Strength, Multilayer Ceramics for Compact Pulsed Power Applications*, in *International Pulsed Power Conference*. 1999: Monterey, CA.
2. Jackson, N.F., *Dielectric Materials in Thin Film Capacitors.* Physics Education, 1968. **3**: p. 253.
3. Kasap, S.O., *Principles of Electronic Materials and Devices*. 2006, New York: McGraw Hill.
4. Kingery, W.D., H.K. Bowen, and D.R. Uhlmann, *Introduction to Ceramics*. 2 ed. 1976: John Wiley & Sons, Inc.
5. Moulson, A.J. and J.M. Herbert, *Electroceramics*. 2 ed. 2003, Hoboken, NJ: John Wiley & Sons Ltd.
6. Vermeer, J., *The Impulse Breakdown Strength of Pyrex Glass.* Physica XX, 1954: p. 313.
7. Vermeer, J., *On the Relation Between Ionic Conductivity and Breakdown Strength of Glass.* 1956. **Physica XXII**: p. 1269.
8. Vermeer, J., *The Electric Strengths of Glasses With Different Sodium Contents.* Physica XXII, 1956: p. 1247.
9. Tunkasiri, T. and G. Rujijanagul, *Dielectric strength of fine grained barium titanate ceramics.* Journal of Materials Science Letters, 1996. **15**: p. 1767.
10. Young, A., et al., *Effect of Liquid-Phase Sintering on the Breakdown Strength of Barium Titanate.* The American Ceramic Society, 2007. **90**(1504).
11. Zhang, Q., et al., *Improved Energy Storage Density in Barium Strontium Titanate by Addition of BaO–SiO2–B2O3 Glass.* The American Ceramic Society, 2009. **92**(1871).
12. Gerson, R. and T.C. Marshall, *Dielectric Breakdown of Porous Ceramics.* Journal of Applied Physics, 1959. **30**(11): p. 1650.
13. Lee, H., et al., *Dielectric Breakdown of Thinned BaO-Al2O3-B2O3-SiO2 Glass.* The American Ceramic Society, 2010. **Accepted for publication**.
14. Smith, N.J., et al., *Alkali-free glass as a high energy density dielectric material.* Materials Letters, 2009. **63**: p. 1245.
15. Austen, A.E.W. and S. Whitehead. *The Electric Strength of Some Solid Dielectrics*. in *Royal Society of London. Series A, Mathematical and Physical Sciences*. 1940.
16. Frohlich, H., *Dielectric Breakdown in Solids.* p. 411.
17. Hippel, A.V. and R.J. Mauer, *Electric Breakdown of Glasses and Crystals as a Function of Temperature.* Physics Review, 1941. **59**.
18. Spierings, G.A.C.M., *Review: Wet Chemical Etching of Silicate Glasses in Hydrofluoric Acid Based Solutions.* Journal of Materials Science, 1993. **28**: p. 6261.
19. Brassard, D., L. Ouellet, and M.A.E. Khakani, *Room-Temperature Deposited Titanium Silicate Thin Films for MIM Capacitor Applications.* IEEE ELECTRON DEVICE LETTERS, 2007. **28**(4): p. 261.
20. Brassard, D., et al., *Compositional effect on the dielectric properties of high-k titanium silicate thin films deposited by means of a cosputtering process.* The Journal of Vacuum Science and Technology, 2006. **24**(3).

21. Kuo, D.H. and C.H. Chien, *Growth and properties of sputtered zirconia and zirconia–silica thin films.* Thin Solid Films, 2003. **429**: p. 40.
22. Wasa, K., M. Kitabatake, and H. Adachi, *Thin Film Materials Technology*. 2004, New York: Andrew Publishing.
23. Weibull, W., *A Statistical Distribution Function of Wide Applicability.* Journal of Applied Mechanics, 1951: p. 293.
24. Mattox, D.M., *Handbook of Physical Vapor Deposition (PVD) Processing*. 1998, Westwood, NJ: Noyes Publications.
25. Ohring, M., *The Material Science of Thin Films*. 1992, New York: Academic Press, Inc.
26. Smentkowski, V.S., *Review: Trends in Sputtering.* Progress in Surface Science, 2000. **64**: p. 1.
27. Smith, D.L., *Thin-Film Deposition, Principles and Practices.* 1995, McGraw Hill, Inc.: New York.
28. Brauer, G., J. Szczyrbowski, and G. Teschner, *New Approaches for Reactive Sputtering of Dielectric Materials on Large Scale Substrates.* Journal of Non-Crystalline Solids, 1997. **218**: p. 19.
29. Varshneya, A.K., *Fundamentals of Inorganic Glasses*. 2 ed. 2006: Alden Group Ltd.
30. Flowers, D.L., *Dielectric Breakdown and Device Evaluation of Fritted Glass Compositions.* Journal of Electrochemical Society, 1981. **128**(10): p. 2179.
31. Pliskin, W.A., *The Evaluation of Thin Film Insulators.* Thin Solid Films, 1968. **2**: p. 1.
32. Pliskin, W.A., et al., *Properties of Insulating Thin Films Deposited by RF Sputtering.* IBM Journal, 1967: p. 461.
33. Pliskin, W.A. and H.S. Lehman, *Structural Evaluation of Silicon Oxide Films.* Journal of The Electrochemical Society, 1965. **112**(10): p. 1013.
34. Herrmann, R., et al., *Influence of an R.F. Plasma on the Optical and Structural Properties of Vacuum-Deposited Dielectric Coatings.* Thin Solid Films, 1985. **127**: p. 351.
35. Martin, P.J., *Review: Ion-based methods for optical thin film deposition.* Journal of Materials Science, 1998.
36. Pitt, C.W., F.R. Gfeller, and R.J. Stevens, *R.F. Sputtered Thin Films for Integrated Optical Components.* Thin Solid Films, 1975. **26**: p. 27.
37. Hawthorne, J.A., *Sputtered Titania Borosilicate Glass Films.* Thin Solid Films, 1991. **202**: p. 321.
38. Titchmarsh, J.G. and P.A.B. Toombs, *Bismuth-Based Glasses for Thin-Film Capacitors Deposited by RF Sputtering.* The Journal of Vacuum Science and Technology, 1969. **7**(1).
39. Frohlich, H., *On the Theory of Dielectric Breakdown in Solids.* 1946: p. 521.
40. Matsunami, N., et al., *Energy Dependence of the Ion-Induced Sputtering Yeilds of Monoatomic Solids* Atomic Data and Nuclear Data Tables, 1984. **31**: p. 1.
41. Solymar, L. and D. Walsh, *Electrical Properties of Materials*. 7 ed. 2004, New York, NY: Oxford University Press.
42. Dissado, L.A., et al., *Weibull Statistics in Dielectric Breakdown; Theoretical Basis, Applications and Implications.* IEEE Transactions on Electrical Insulation, 1984. **E1-19**(3): p. 227.
43. Heimann, P.A., *An Operational Definition for Breakdown of Thin Thermal Oxides of Silicon.* IEEE Transactions on Electron Devices, 1983. **30**(10): p. 1366.
44. Zoschke, K., et al., *Evaluation of Micro Structured Glass Layers as Dielectric- and Passivation Material for Wafer Level Integrated Thin Film Capacitors and Resistors.* IEEE, 2007: p. 566.

45. Nix, W.D., *Mechanical Properties of Thin Films.* Metallurgical Transactions A, 1988. **20A**: p. 1989.
46. Atuchin, V.V., et al., *X-ray photoelectron spectroscopy study of beta-BaB2O4 optical surface.* Applied Surface Science, 2004. **223**: p. 352.
47. Smith, G.C., *Evaluation of a simple correction for the hydrocarbon contamination layer in quantitative surface analysis by XPS.* Journal of Electron Spectroscopy, 2005. **148**: p. 21.
48. Chen, C., et al., *Multichannel Mueller matrix ellipsometer based on the dual rotating compensator principle.* Thin Solid Films, 2004. **455-456**: p. 14.
49. Tompkins, H.G. and W.A. McGahan, *Spectroscopic Ellipsometry and Reflectometry: A Users Guide*. 1999, New York: John Wiley & Sons, Inc.
50. Fujiwara, H., et al., *Assessment of effective-medium theories in the analysis of nucleation and microscopic surface roughness evolution for semiconductor thin films.* Physical Review B 2000. **61**(10832).
51. Tiwald, T., *Sellmeier Dispersion*. 2009.
52. Thornton, J.A., *Influence of Apparatus Geometry and Deposition Conditions on the Structure and Topography of Thick Sputtered Coating.* American Vacuum Society, 1973. **11**(4): p. 666.
53. Davidse, P.D. and L.I. Maissel, *Dielectric Thin Films Through RF Sputtering.* Journal of Applied Physics, 1966. **37**(2): p. 574.
54. Choi, W.K., et al., *Densification of radio frequency sputtered silicon oxide films by rapid thermal annealing.* Journal of Applied Physics, 1998. **83**(4): p. 2308.
55. Shelby, J.E., *Introduction to Glass Science and Technology*. 2 ed. 2005, Cornwall, UK: The Royal Society of Chemistry.